International Journal of Mechanical Sciences 215 (2022) 106917

Contents lists available at ScienceDirect

International Journal of Mechanical Sciences

journal homepage: www.elsevier.com/locate/ijmecsci

Probing the effect of surface parameters and particle size in the diffusion-induced stress of electrodes during lithium insertion

Bo Wang, Katerina E. Aifantis *

Department of Mechanical and Aerospace Engineering, University of Florida, Gainesville, FL, 32608, USA

ARTICLE INFO

Keywords:
Stress evolution
Phase transformation
Surface elasticity
Gradient plasticity
Li-ion batteries

ABSTRACT

Experimental studies have shown that the active particles of electrodes undergo phase transformations during ion-insertion, which are accompanied by diffusion induced stresses that result in fracture at the particle surface. Only a few studies have considered the effect that the surface stress has on the diffusion-induced stress that occurs in electrode materials that undergo elastic deformations during ion-insertion, while no studies have accounted for the effect of surface stresses in the case when plastic deformation is also present. In addition, there are only few comprehensive studies on the competing effect between the surface stress and the strain gradient during ion diffusion. The present work sheds light on the effect that the particle size has on the stresses generated due to the phase transformations that take place during ion-insertion by accounting for the surface residual stress with strain gradient elasticity or strain gradient plasticity. Due to the presence of surface stresses, the stress on the particle outer surface can be significantly reduced. In particular, when the residual surface stress and the surface elastic modulus are both positive, the hoop stress at the outer surface remains compressive, whereas tensile stresses are required for crack formation. This work, therefore, indicates that surface modification could be an effective approach for improving the structural integrity of electrodes during the lithiation process. The additional consideration of strain gradients further reduces the value of the equivalent plastic strain for elasto-plastic electrode particles. These findings render prospective insights for designing next-generation mechanically stable phase transforming electrode materials.

1. Introduction

Li-ion batteries (LIBs) have gained increasing interest and attention from researchers worldwide over the past two decades. Intensive efforts are devoted in developing electrodes with a superior performance such as high energy and power densities, as well as long cycle life. One of the critical challenges in advancing energy storage technology is the mechanical degradation/fracture that occurs during normal operation of a battery, which results from phase transformations and volume changes that occur during charging/discharging. Fracture of the active particles (particles that accept the Li-ions) can lead to capacity loss and ultimately failure of the battery. Due to the constant exchange of ions, it is anticipated that diffusion-induced stress (DIS) is one of the main factors causing capacity fade in electrode materials. One of the promising means to address these challenges is to exploit nano-structured or nano-sized materials, as experiments have shown that they allow for a significant improvement in the rate capability, cycle life and mechanical stability. For example, nanostructured $LiFePO_4$ powders (cathode material) can provide a specific capacity of 123 mAh/g and 157 mAh/g at discharge rates of 10 C and 1 C with less than 0.08% fade per cycle, respectively [1]. In the case of anodes, the first nano-Si composite materials obtained by mixing nanometer-scale (78 nm) pure Si powder (anode active material) and carbon black exhibited over 1700 mAh/g reversible capacity at the tenth cycle [2]. Si exhibits volume expansions that are over 300% upon the formation of lithium alloys, which leads to fracture. An interesting and intriguing phenomenon is that there exists a critical size below which no pulverization or fracture occurs. For nanospherical Si particles, in situ experiments showed that the critical diameter is about 150 nm [3], while for Si thin film electrodes, the critical thickness is reported to be 100–200 nm [4]. In-situ and ex-situ experiments have shown that fracture occurs, upon the first maximum Li-insertion, at the external surface of Si or Sn particles [5,6]. Numerous nano-Si based anodes have, therefore, been fabricated which allow for capacities over 1000 mAh/g for over 100 cycles. In addition to nanospheres [7–12] and nanowires [13–16], other nanostructures such as nanotubes [17–19], nanopillars [20–22] and nanofilms [23,24] have been employed and they have demonstrated a highly reversible lithium storage and excellent high-rate capability.

* Corresponding author.
E-mail address: kaifantis@ufl.edu (K.E. Aifantis).

https://doi.org/10.1016/j.ijmecsci.2021.106917
Received 23 April 2021; Received in revised form 31 October 2021; Accepted 31 October 2021
Available online 18 November 2021
0020-7403/Published by Elsevier Ltd.

Although extensive electrochemical research has been carried out for various nanomaterials, a fundamental and comprehensive understanding of the deformation and fracture mechanisms has yet to be achieved. Early mechanics studies focused on using linear elasticity and linear elastic fracture mechanics for modeling stress and crack propagation during maximum ion-insertion, without explicitly accounting for Li-ion diffusion, and were able to provide preliminary design criteria for mechanically stable anodes [25–28]. Generally speaking, small electrode particles experience small DISs [29–32] because the smaller the particle, the more uniform the Li concentration in the electrode and consequently the smaller the concentration gradient inside the electrode. When the size is down to the nanoscale, the properties of these nanomaterials can be quite different since many experiments suggest that size reduction at the nanoscale is often accompanied by changes in strength, hardness, or ductility when compared to their bulk counterparts [29,33–36], due to the high surface/bulk ratio of nanomaterials. The local environment of atoms at a free surface is remarkably different from that of atoms inside the bulk material. For atoms near the free surface, there is a redistribution of electronic charges close to the surface due to missing bonds. Thus, the surface layers cannot have the same elastic properties as those in the bulk. As a result, the energy associated with those atoms is also different, which is often termed surface free energy. Since only a few layers of atoms are near the surface in macroscopic materials, the ratio of the volume occupied by those atoms to the total volume of the bulk is extremely small and this part of the excess energy is often neglected. When it is down to the nanoscale, however, this excess energy portion becomes significant. Hence, it can be expected that surface energies and the resulting surface stresses would have a significant impact on the DISs of nanoscale active particles. In particular, when this surface effect is taken into account, the stress status might be different from that predicted from traditional continuum mechanics. In [30] the effects of surface stresses were examined and it was found that when surface mechanics are considered, a compressive stress develops on the surface instead of traction-free conditions, thus helping prevent crack growth. The DIS in spherical core–shell electrodes was also investigated in [37] by including the effects of surface/interface stresses, and it was shown that DISs were significantly reduced by the residual surface tension, making the electrodes more resistant to brittle fracture.

The main cause of fracture in electrode materials are the high stresses that develop due to lithium intercalation/deintercalation. Many models have been developed to capture this DIS [12,30,31,38–46], based on the early model of [47] where the transverse stresses developed in a thin plate during mass transfer were modeled in analogy to thermal stresses. However, only a few models take into account the effect of phase transformations during lithium insertion.

The stress evolution in electrode particles undergoing phase separation has been elaborately studied in previous works [48–53]. When the electrode underwent elastic deformation during lithium insertion, it was found that the radial stress was always tensile, while the hoop stress was tensile in the core region and compressive in the shell [50]. And these stress states were the opposite for the de-insertion process [48]. For some high-capacity electrodes undergoing large volume expansions during Li-insertion, plastic deformation can take place. Both in-situ measurements [54] and molecular dynamic simulations [55] of the stress evolution in Si anodes during lithiation/delithiation have revealed that yielding and plastic flow occur. When plastic deformation was assumed, the radial stress showed a transition from tension in the initial stages to compression at the later stages, while the surface hoop stress changed from compression to tension in the later stages [51–53,55]. These models, however, did not capture the size effects which have been observed by many experiments.

It was shown in [56] that the effect of the hydrostatic stress is significant for electrodes undergoing elastic deformation during Li-insertion at the micro-scale, while surface/interface stresses cannot be neglected at the nano-scale. In [57] the size-dependent migration of two-phase lithiation in a 40 nm spherical Si particle was studied. The model incorporated effects of surface/interface elasticity and it was found that larger radial compression was predicted in a smaller particle while the hoop stress was independent of the particle size. As a result, the phase interface velocity was slower in the smaller particle when plasticity was considered. In addition to capturing the stress reversal in the hoop stress [3], a strong size dependence of the J-integral near the crack tip was found, which showed that smaller particles can avert fracture. However, similar size effects within a plasticity framework have not been captured.

The most appropriate continuum models that can be used for capturing size effects are those of gradient elasticity [58–60] and gradient plasticity [61–65]. The first applications of such theories for electrode modeling was done in [66] where it was possible to capture size-dependent miscibility gaps by coupling gradient elasticity with a chemo-mechanical theory for phase transforming species under diffusion. A similar gradient elasticity framework was used to determine the critical size of silicon nanowires that would inhibit fracture [67], by considering two-phase lithiation. It was shown that a larger internal length lead to less sharp interfaces and faster diffusion. It was also shown that the DISs due to lithium insertion were pretty high, implying that plasticity is likely to take place at the early stages of lithiation [66]. Gradient elasticity has also been applied recently for single phase lithiation [68] in order to study the effects of particle size on DIS within a purely gradient elasticity framework. The main finding was that the DIS became higher as the internal scale (length) increased. Gradient damage mechanics were also successfully employed to predict the interparticle spacing between active particles that would limit damage, and predict that graphene was the most promising matrix material to stabilize the volume expansion of Sn anodes, which was in accordance with experiments [69].

It has to be noted that the majority of the effort, thus far, has concentrated on capturing either surface effects or gradient elasticity effects. A comprehensive study of both effects has yet to be achieved. Also, as it has been aforementioned, plastic deformation may occur for electrodes under dramatic volume variations, but has yet to be accounted for. In this work, both the surface effects and gradient effects (elastic and plastic) on DIS will be considered. Our model is applied to Li-ion batteries, but it can be used for any type of ion-batteries, including Na-ion batteries.

2. Modeling and simulation results

The charge and discharge of LIB electrodes is accompanied by volume changes. The volume expansion depends on the storage mechanism. The lithiation of conventional cathode active materials is done via intercalation and the volume changes are usually very small. For instance, $LiFePO_4$ shrinks approximately 7% after full delithiation [70,71]. For anode materials, the lithiation is done either by alloying or conversion mechanisms. Particularly, for Si, which can store over 4.4 Li mols (per Si mol) upon maximum lithiation, its volume expansion can be as high as 420%, and as a result, considerable mechanical stress is built up during lithiation or delithiation. In order to model the DIS, for both anodes and cathodes, suitable constitutive equations are needed.

Since cathodes undergo a lower volume change during lithiation they are assumed to remain elastic during intercalation. Therefore, small deformation based on linear elasticity theory can be applied. Anodes, however, undergo larger volume changes and the resulting internal stresses would exceed the yield criterion. As a result, plastic deformation can occur and plastic models would be more appropriate for anode materials.

In classical continuum mechanics, the constitutive relations do not include any characteristic (internal) length. Therefore, classical theories cannot predict the dependence of material behavior on the sample size. To have a better understanding of the material properties at the micro

and nano scale, realistic models must take size effects, surface and interface effects into account. Non-local theories bridge the gap between classical elasticity/plasticity theory and molecular dynamic simulation since new constitutive models which take size effects into consideration can be established under classical continuum mechanics frameworks. These models can be obtained by the principle of virtual power/work. Another important feature of these models is their intimate relationship with the Ginzburg–Landau theory of phase transitions and, for fluids, van der Waals' theory. Many researchers extended these models to other fields (gradient damage/diffusion, etc.). They are widely used in materials science for modeling microstructure evolution/solidification, damage/fracture etc. This approach is called the phase field approach, as it uses a smeared interface instead of a discrete interface. The internal length agrees with the actual intrinsic thickness of the physical interfaces. Both nonlocal continuum models and the phase field models can eliminate singularities in the study of structural defects (dislocations, disclinations) in elasticity with higher-order gradients.

Many electrode materials exhibit phase segregation into lithium-rich (Li-rich) and lithium-poor (Li-poor) phases respectively during lithium insertion and de-insertion. For these materials, a core–shell model is often used to model the diffusion process. It is often assumed that the phase boundary moves in the radial direction and the expansion is isotropic. During Li^+ insertion, the core and shell would consist of Li-rich and Li-poor phases, respectively. Traditional sharp interface models lead to discontinuous concentration and stress profiles, and the discontinuities appear at the interface. As a result, the moving phase boundary needs to be tracked and specific boundary conditions need to be applied at the phase interface. To model the sharp phase boundary, an alternative approach is by using the Cahn–Hilliard type diffusion equation. The model can be derived via a variational formulation approach. It is worth noting that the models within a local continuum framework inherently fail to address the strain softening behavior as they result in mesh-dependent results and give further rise to zero energy dissipation in the limit of vanishingly small mesh sizes [72,73]. Therefore, many non-local continuum theories have been proposed and developed, aiming in overcoming these difficulties [74–77]. Herein strain-gradient theories, which are capable of overcoming the issues due to strain softening, will be employed to capture the size effects [59,78]. The surface effects are captured by employing surface elasticity theories [79,80].

2.1. DISs under elastic deformation

For the case of pure elastic deformation of the electrode during ion insertion, the system (total) free energy is given by:

$$\Psi = \int_{\Omega} \psi^b dV + \int_{\Gamma} \psi^s dS \tag{1}$$

Where ψ^b is the bulk free energy density, i.e., free energy per unit reference volume, and ψ^s is the surface free energy density, i.e. free energy per unit reference area. The electric contributions to the energy are not considered. By not including all terms into the free energy, the problem is simplified. The bulk free energy density is :

$$\psi^b = \psi^b(\boldsymbol{\varepsilon}, \nabla\boldsymbol{\varepsilon}, c, \nabla c) \tag{2}$$

where c denotes the local nominal concentration (the number of lithium ions, in moles per unit volume) of the diffusing species, and ∇c is the concentration gradient of the chemical species (Li-ions). The linear strain tensor is given by : $\boldsymbol{\varepsilon} = \frac{1}{2}\left[\nabla \boldsymbol{u} + (\nabla \boldsymbol{u})^T\right]$ or $\varepsilon_{ij} = \frac{1}{2}\left(\frac{\partial u_i}{\partial x_j} + \frac{\partial u_j}{\partial x_i}\right)$ where $\boldsymbol{u}$ is the displacement field. The infinitesimal strain tensor is adopted, and it should satisfy the displacement compatible conditions. The gradient of the strain field $\nabla\boldsymbol{\varepsilon}$ is a third order tensor, given by: $\varepsilon_{ij,k} = \frac{\partial \varepsilon_{ij}}{\partial x_k}$. It is reminded that $\boldsymbol{u}$ is the displacement of the particle located at x in the reference configuration (the initial stress-free configuration). The bulk free energy density is comprised of two parts:

$$\psi^b = \psi^m + \psi^c \tag{3}$$

The energy density due to mechanical deformation is:

$$\psi^m = \psi^m(\boldsymbol{\varepsilon}^e, \nabla\boldsymbol{\varepsilon}^e) = \psi^e(\boldsymbol{\varepsilon}^e) + \psi^g(\nabla\boldsymbol{\varepsilon}^e) \tag{4}$$

Assume that the deformation is small so that the binary solid can be considered as being linearly elastic, the elastic strain energy density is $\psi^e(\boldsymbol{\varepsilon}) = \frac{1}{2}\boldsymbol{\varepsilon}^e : \mathbb{C} : \boldsymbol{\varepsilon}^e$, and the elastic strain tensor is $\boldsymbol{\varepsilon}^e = \boldsymbol{\varepsilon} - \boldsymbol{\varepsilon}^c$. $\boldsymbol{\varepsilon}^c$ is the chemically induced strain tensor and is locally different due to different local concentrations. For a homogeneous and isotropic material, hydrostatic dilatation is assumed and it is given by $\boldsymbol{\varepsilon}^c = \alpha\left(c^* - c_0^*\right)\mathbf{1}$ where $\mathbf{1}$ is a third-order identity tensor, $\mathbb{C}$ is a fourth-order elasticity tensor, given by $\boldsymbol{C}_{ijkl}(c) = \lambda(c)\delta_{ij}\delta_{kl} + \Lambda(c)\left(\delta_{ik}\delta_{jl} + \delta_{il}\delta_{jk}\right)$ with $\lambda(c)$ and $\Lambda(c)$ being concentration-dependent Lamé constants, and δ_{ij} is the Kronecker delta. c_0^* is a reference concentration, usually set as 0. α is the dilatation coefficient (analogous to the thermal expansion coefficient), and is given by:

$$\alpha = \frac{1}{3}\Xi c_{\max} \tag{5}$$

where Ξ is the partial molar volume of lithium ions and $c_{\max}$ is the maximum concentration in the Li/electrode system (i.e. at the fully lithiated state), c_0 is the initial concentration, c^* is the normalized/relative concentration, $c^* = \frac{c}{c_{\max}}$. The normalized concentration is used to characterize the relative saturation level of Li in an electrode ("0" means no ions and "1" means maximum Li-ion insertion). The energy contribution due to the strain gradient is given by:

$$\psi^g(\nabla\boldsymbol{\varepsilon}^e) = \frac{{l_\varepsilon}^2}{2}\nabla\boldsymbol{\varepsilon}^e : \mathbb{C} : \nabla\boldsymbol{\varepsilon}^e \tag{6}$$

where l_ε is the internal length scale.

The energy contribution due to the concentration gradient on the diffuse interfaces cannot be neglected. The chemical energy density is given by:

$$\psi^c = \psi^c(c, \nabla c) = \psi^{ch} + \psi^{cg} \tag{7}$$

where ψ^{ch} is the homogeneous chemical free energy density (free energy density of a homogeneous system of uniform concentration). The chemical contribution to the stored energy is assumed to have the form:

$$\psi^{ch} = \psi^{ch}(c) = RTc_{\max}\left[c^*\ln c^* + \left(1-c^*\right)\ln\left(1-c^*\right) + \chi c^*\left(1-c^*\right)\right] + \mu_0 c \tag{8}$$

Here R is the gas constant (8.314 J/K/mol), T is the absolute temperature, RT denotes the specific molar energy (the energy per mole), μ_0 is a reference value of the chemical potential of the diffusing species (set as 0 since it will not affect the diffusion behavior), and χ is the constant partial molar volume. The contributions due to the sharp concentration gradient are usually neglected. Note that $\mu_0 c$ corresponds to the internal energy due to the presence of lithium ions in their stable sites, not interacting with each other. The interface between the lithium-rich and lithium-poor Li-rich and Li-poor volumes is related to misfits in the crystal structure. Therefore, a penalty term involving a norm of the gradient of the phase-field is added into the free energy of the system as:

$$\psi^{cg} = \frac{\kappa}{2}|\nabla c|^2 \tag{9}$$

where κ is the gradient energy coefficient [81,82]. The surface free energy is dependent on the surface concentration c_s and the total surface strain ε^s. Based on surface elasticity theory, the following surface free energy is adopted:

$$\psi^s = \gamma_0 + \tau^s : \left(\boldsymbol{\varepsilon}^s - \boldsymbol{\varepsilon}^0\right) + \frac{1}{2}\left(\boldsymbol{\varepsilon}^s - \boldsymbol{\varepsilon}^0\right) : \mathbb{C}^s : \left(\boldsymbol{\varepsilon}^s - \boldsymbol{\varepsilon}^0\right) \tag{10}$$

Here variables with a superscript "s" are associated with the surface. ε^0 is the surface eigen-strain and $\varepsilon^s - \varepsilon^0$ gives the surface elastic strain, τ^s is the surface residual stress, $\mathbb{C}^s$ is the surface elastic stiffness tensor, and γ_0 represents the undeformed surface energy. The surface strain is defined as:

$$\boldsymbol{\varepsilon}^s = \frac{1}{2}\left[\nabla_s \boldsymbol{u} + \left(\nabla_s \boldsymbol{u}\right)^T\right] \tag{11}$$

$\nabla_s \boldsymbol{u} = \nabla \boldsymbol{u} \cdot \mathbb{P}$ is the surface gradient of displacement, $\mathbb{P} = \boldsymbol{I} - n \otimes \boldsymbol{n}$ is the tangential projection tensor, $\boldsymbol{I}$ is the second-order identity tensor, $\otimes$ represents a dyad, and $\boldsymbol{n}$ is a unit vector normal to the surface (the projection tensor of an arbitrary point on a surface). The surface gradient in index form is: $\nabla_s \boldsymbol{u} = D_j u_i = \frac{\partial u_i}{\partial x_k}\left(\delta_{kj} - n_j n_k\right)$. The surface compositional (eigen-)strain can be written as:

$$\boldsymbol{\varepsilon}^0 = \alpha_s \left(c_s{}^* - c_{s0}{}^*\right) \boldsymbol{I} \tag{12}$$

where $c_s{}^*$ is the normalized surface concentration, $c_{s0}{}^*$ is the reference surface concentration (usually set as 0), and α_s is the compositional strain coefficient of the surface. For the sake of simplicity, α_s is taken the same as the dilatation coefficient α in the bulk.

The energy supply due to mass transport at the current time t is given by:

$$P = \int_0^t \int_\Omega \frac{\partial c}{\partial t} \mu dt dV + \int_0^t \int_{\partial\Omega^i} \boldsymbol{J} \cdot \boldsymbol{n}_i \mu dt dS \tag{13}$$

where $\boldsymbol{J}$ is the Li-ion flux, Ω is the volume of the electrode (only one particle is considered), μ is the chemical potential of lithium ions, $\partial\Omega^i$ is the boundary for the lithium ion flux, and $\boldsymbol{n}_i$ is the unit normal vector of $\partial\Omega^i$. dV and dS in the integral terms represent the volume and surface integral, respectively. The gradient of the chemical potential is the chemical driving force for diffusion, i.e., the gradient of the diffusional potential of Li μ serves as the driving force for Li diffusion:

$$\boldsymbol{J} = -\boldsymbol{M} \nabla \mu \tag{14}$$

where $\boldsymbol{M}$ is the mobility tensor, which is generally a function of Li concentration c. For isotropic materials, it is assumed to have the form:

$$\boldsymbol{M} = c^* \left(1 - c^*\right) M \boldsymbol{1} \tag{15}$$

where M is the solute mobility and is independent of time. The diffusivity coefficient D is given by: $D = MRT$.

The work done by external loads is given by:

$$W = \int_\Omega \boldsymbol{b} \cdot \boldsymbol{u} dV + \int_{\partial\Omega^t} \boldsymbol{t} \cdot \boldsymbol{u} dS + \int_\Gamma \boldsymbol{p} \cdot \boldsymbol{u} ds + \int_0^t \int_{\partial\Omega^i} i \mu dt dS \tag{16}$$

where $\boldsymbol{b}$ is the body force density in the material, $\boldsymbol{t}$ is the surface force per unit area, often referred to as traction, $\boldsymbol{p}$ is the external force density along the curve Γ per unit length in the material configuration, i is the concentration flux across $\partial\Omega^i$, and $\partial\Omega^t$ is the boundary for the surface traction. ds in the integral term represents the line integral. The regularized total potential energy for the given body Ω subject to boundary conditions is given by:

$$\Pi = \Psi - P - W \tag{17}$$

The principle of virtual power reads as [83,84]:

$$\begin{aligned} \delta\dot{\Pi} = &\int_\Omega (\boldsymbol{\sigma}^c : \delta\dot{\boldsymbol{\varepsilon}}) dV + \int_{\partial\Omega^s} (\boldsymbol{\sigma}^s : \delta\dot{\boldsymbol{\varepsilon}}^s) dS + \int_{\partial\Omega^\tau} (\boldsymbol{\tau} : \delta\nabla\dot{\boldsymbol{\varepsilon}}) dS \\ &- \int_\Omega \frac{\partial c}{\partial t} \delta\mu dV + \int_\Omega \boldsymbol{J} \cdot \delta\nabla\mu dV \\ &- \int_\Omega \boldsymbol{b} \cdot \delta\dot{\boldsymbol{u}} dV - \int_{\partial\Omega^t} \boldsymbol{t} \cdot \delta\dot{\boldsymbol{u}} dS \\ &- \int_\Gamma \boldsymbol{p} \cdot \delta\dot{\boldsymbol{u}} ds - \int_{\partial\Omega^i} i\delta\mu dS \end{aligned} \tag{18}$$

where $\partial\Omega^s$ and $\partial\Omega^\tau$ are the boundaries for the surface stress and the higher order stress respectively. $\delta\dot{\Pi} = 0$ must hold for all admissible variations. Integrating by parts and applying Green's theorem, results in the following governing equations and boundary conditions for the coupled system:

$$\begin{cases} \boldsymbol{t} = (\boldsymbol{\sigma}^c - \nabla \cdot \boldsymbol{\tau}) \cdot \boldsymbol{n}_t - \left(\nabla_s \cdot \boldsymbol{\sigma}^s\right) + (\boldsymbol{\sigma}^s : \mathbb{K}) \boldsymbol{n}_t \text{ on } \partial\Omega^t \\ \nabla \cdot ((\boldsymbol{\sigma}^c - \nabla \cdot \boldsymbol{\tau})) + \boldsymbol{b} = \boldsymbol{0} \text{ in } \Omega \backslash \partial\Omega^t \\ \boldsymbol{u} = \bar{\boldsymbol{u}} \text{ on } \partial\Omega^u \\ i = \boldsymbol{J} \cdot \boldsymbol{n}_i \text{ on } \partial\Omega^i \\ \frac{\partial c}{\partial t} + \nabla \cdot \boldsymbol{J} = 0 \text{ in } \Omega \backslash \partial\Omega^i \\ \mu = \bar{\mu} \text{ on } \partial\Omega^\mu \\ \boldsymbol{p} = \boldsymbol{\sigma}^s \cdot \boldsymbol{n}_\Gamma \text{ on } \Gamma \end{cases} \tag{19}$$

where $\partial\Omega^u$ and $\partial\Omega^\mu$ are boundaries for the displacement and chemical potential, respectively. $\mathbb{K}$ is the curvature tensor (curvature tensor of the surface), while $\boldsymbol{n}_t$ and $\boldsymbol{n}_\tau$ are the unit normal vectors of $\partial\Omega^t$ and $\partial\Omega\tau$, respectively. The displacement and the chemical potentials remain constant values $\bar{\boldsymbol{u}}$ and $\bar{\mu}$ across the boundaries. (In particular, for a spherical electrode particle, it often means zero displacement and zero ion flux at the center.) the state variables are:

$$\boldsymbol{\sigma}^c = \frac{\partial \psi}{\partial \boldsymbol{\varepsilon}}, \ \boldsymbol{\tau} = \frac{\partial \psi}{\partial \nabla \boldsymbol{\varepsilon}}, \ \boldsymbol{\sigma}^s = \frac{\partial \psi}{\partial \boldsymbol{\varepsilon}^s} \tag{20}$$

where $\boldsymbol{\sigma}^c$ is the classical stress tensor

$$\boldsymbol{\sigma}^c = \frac{\partial \psi}{\partial \boldsymbol{\varepsilon}} = \frac{\partial \psi^e}{\partial \boldsymbol{\varepsilon}} = \mathbb{C} : \boldsymbol{\varepsilon}^e \tag{21}$$

$\boldsymbol{\tau}$ is the higher order stress due to the strain gradient, and $\boldsymbol{\sigma}^s$ is the surface stress tensor, given by:

$$\boldsymbol{\sigma}^s = \frac{\partial \psi}{\partial \boldsymbol{\varepsilon}^s} = \frac{\partial \gamma}{\partial \boldsymbol{\varepsilon}^s} = \boldsymbol{\tau}^s + \mathbb{C}^s : \left(\boldsymbol{\varepsilon}^s - \boldsymbol{\varepsilon}^0\right) \tag{22}$$

For isotropic materials, the surface stress is

$$\boldsymbol{\sigma}^s = \boldsymbol{\tau}^0 \boldsymbol{1} + \mathbb{C}^s : \boldsymbol{\varepsilon}^s = \boldsymbol{\tau}^0 \boldsymbol{1} + \lambda_s \mathrm{tr}\left(\boldsymbol{\varepsilon}^s\right) 1 + 2\Lambda_s \boldsymbol{\varepsilon}^s \tag{23}$$

where τ^0 is a constant surface stress that is strain-independent (deformation-independent residual surface stress), λ^s and Λ^s are surface Lamé constants. For isotropic spherical particles deforming uniformly, the surface stress may be written as:

$$\sigma^s_{\theta\theta} = \tau^0 + K^s \varepsilon^s_{\theta\theta} \tag{24}$$

where K^s is the surface modulus, $\varepsilon^s_{\theta\theta}$ is the hoop surface strain component, τ^0 is the residual surface tension/compression under unrestrained conditions and $K^s = 2\left(\lambda_s + \Lambda_s\right)$. The chemical potential is defined via the variational derivative of the total free energy with respect to the ion concentration, i.e,

$$\mu = \frac{\delta \psi}{\delta c} = \frac{\partial \psi}{\partial c} - \nabla \cdot \left(\frac{\partial \psi}{\partial \nabla c}\right) \tag{25}$$

It should be noted that the diffusive model is adopted for the ion diffusion process. Unlike sharp interface models, for electrode materials that undergo phase transformations, the concentration profile obtained from the phase field model is continuous across the body. For sharp interface models, there is a concentration jump at the phase interface. Therefore, additional boundary conditions are needed. The discontinuous concentration profile also leads to a discontinuous chemical potential. Consequently, additional state variables (surface concentration and surface chemical potential) and boundary conditions are needed for those sharp interface models. The phase field model reduces the complexity of the formulation.

To avoid numerical difficulties caused by the logarithmic terms and ensure numerical efficiency, polynomial approximations are usually adopted in most studies [85–88]. In this work, the following polynomial approximation is used:

$$\psi_{poly}\left(c^*\right) = a_0\left(c^* - \frac{1}{2}\right)^4 + a_1\left(c^* - \frac{1}{2}\right)^2 + a_2 \tag{26}$$

with a_0, a_1, a_2 being appropriate fit parameters. By definition, Eq. (26) is a convex function and symmetric around $c^* = \frac{1}{2}$. The equilibrium

concentrations are denoted by $c_r{}^*$ and $c_p{}^*$, and the subscripts "r" and "p" represent the Li-rich and Li-poor phases respectively. The physical meaning is that $c_r{}^*$ and $c_p{}^*$ correspond to the local minima of the chemical free energy density under stress-free conditions. For the sake of simplicity, constant mobility instead of degenerated mobility (i.e., $\boldsymbol{M} = M\mathbf{1}$) is employed. In the current study, $\chi = 4.45$ and the equilibrium concentrations are $c_r{}^* = 0.99$ and $c_p{}^* = 0.01$. As a result, the fit parameters are: $a_0 = 7.67$, $a_1 = -3.64$, $a_2 = 0.42$ [89].

To solve for the diffusion, suppose the electrode is under galvanostatic operation. The particle is charged galvanostatically, with a uniform lithium flux through its free surface

$$M\frac{\partial \mu}{\partial r}\Big|_{r=\rho} = i \text{ on } \partial\Omega^i \tag{27}$$

Here i is the applied current density (per unit area) on the ion flux boundary $\partial\Omega^i$, F is Faraday's constant (96 485 sA/mol), z is the valence number of a Li-ion ($z = 1$, the charge per one ion lithium), and ρ is the radius of the active particle. The variational boundary condition is given by:

$$\kappa\nabla c \cdot \boldsymbol{n}_c = 0 \text{ on } \partial\Omega \tag{28}$$

with $\boldsymbol{n}_c$ being the outward unit normal to the outer boundary $\partial\Omega$. It should be noted that this boundary condition comes from the variational derivation. It will not appear in the weak formulation directly. The weak form of the diffusion equation is given as:

$$\begin{aligned}\int_\Omega \frac{\partial c^*}{\partial t} v dV &= \int_{\partial\Omega^i} iv dS - \int_\Omega M\nabla\mu\nabla v dV\\ \int_\Omega \mu w dV &= \int_\Omega RT\left[4a_0\left(c^* - \frac{1}{2}\right)^3 + 2a_1\left(c^* - \frac{1}{2}\right)\right] w dV\\ &\quad - \int_\Omega \kappa c_{\max}\nabla c^*\nabla w dV\end{aligned} \tag{29}$$

where v and w are arbitrary test functions.

In the present study, the aim is to study the size effect and surface effect. The potential changes due to the stress field are neglected. The formulation here does not seek to address the DIS variations due to material softening. In this regard, concentration-independent Lamé constants are assumed. The weak form of the governing (mechanical equilibrium) equation is given as:

$$\begin{aligned}&-\int_0^\rho \delta u\left(\frac{\partial \sigma_{rr}^e}{\partial r} + \frac{2\left(\sigma_{rr}^e - \sigma_{\theta\theta}^e\right)}{r}\right) r^2 dr\\ &= 2\rho\sigma_{\theta\theta}^s(\delta u)|_{r=\rho} + \int_0^\rho \left(\sigma_{rr}^c\frac{\partial(\delta u)}{\partial r} + 2\sigma_{\theta\theta}^c\frac{\delta u}{r}\right) r^2 dr\\ &+ \int_0^\rho {l_\varepsilon}^2\left(\frac{\partial \sigma_{rr}^c}{\partial r} + \frac{2\left(\sigma_{rr}^c - \sigma_{\theta\theta}^c\right)}{r}\right)\left(\frac{\partial^2(\delta u)}{\partial r^2}r^2 + 2r\frac{\partial(\delta u)}{\partial r} - 2(\delta u)\right) dr\end{aligned} \tag{30}$$

where superscripts "c" and "e" denote, respectively, the component within the classical continuum mechanics framework (without strain gradient effects) and the effective component when the strain gradient effect is taken into consideration. The details are given in Appendix A. For a spherical particle, the constitutive relations for the stresses (σ_{rr}^c and $\sigma_{\theta\theta}^c$) can be written as:

$$\left.\begin{aligned}\sigma_{r_r^c} &= \frac{E}{(1+\upsilon)(1-2\upsilon)}\left[(1-\upsilon)\frac{du}{dr} + 2\upsilon\frac{u}{r} - (1+\upsilon)\alpha c^*\right]\\ \sigma_{\theta_\theta^c} &= \frac{E}{(1+\upsilon)(1-2\upsilon)}\left[\frac{u}{r} + \upsilon\frac{du}{dr} - (1+\upsilon)\alpha c^*\right]\end{aligned}\right\} \tag{31}$$

where E is the Young's modulus, υ is Poisson's ratio, u is the radial displacement, and α is the expansion coefficient of the spherical particle.

By solving the diffusion equation, the concentration can be obtained. Then substituting the constitutive equations into the weak form, the radial displacement can be solved. The numerical implementation details are given in Appendix B. In the simulation, dimensionless/normalized variables are used as shown in Table 1, where $t_0 = \frac{\rho^2}{D}$ is the characteristic time.

Table 1
Normalized/dimensionless variables.

Name	Symbol	Normalized variable
Normalized gradient coefficient	κ^*	$\kappa c_{\max}/\left(RT\rho^2\right)$
Normalized mobility	M^*	$MRTt_0/\rho^2$
Normalized time	t^*	t/t_0
Normalized radial distance	r^*	r/ρ
Normalized stress components	$\sigma_{ij}{}^*$	σ_{ij}/E
Normalized chemical potential	μ^*	$\mu/(RT)$
Normalized ion flux	i^*	$i\rho/\left(zFDc_{\max}\right)$
Normalized partial molar volume	Ξ^*	$\Xi E/(RT)$

2.1.1. Parametric study of surface elasticity for elastic solids

One major difficulty when it comes to surface elasticity is the choice of the surface Lamé constants. Depending on the material, the surface elastic constants can be either positive or negative. This is due to the fact that a surface cannot exist on its own. It is the surface energy plus bulk energy that ensures its overall stability, i.e., the total energy needs to satisfy the positive definiteness condition [90]. The ability of the surface modulus to be negative has been shown via atomistic simulations [91]. Surface moduli are positive/negative if the interface is less/more compliant than the bulk, respectively [92]. To study the effects of these parameters, the DISs of a spherical $LiFePO_4$ particle with a 10 nm ($\rho = 10$ nm) radius are analyzed. Since $LiFePO_4$ is a brittle material, it can be assumed that it undergoes only elastic deformation, during the first lithiation process. Furthermore, no plastic deformation has been observed after the first cycle of $LiFePO_4$. The interface thickness between the unlithiated core and lithiated shell is assumed to be 5 nm [93]. The parameters used are are as follows: $E = 124.5$ GPa, $\upsilon = 0.25$, $M^* = 1$, $i^* = 1$, $\kappa^* = 0.0625$, $\Xi = 2.9 \times 10^{-6}$ m^3/mol, $c_{\max} = 2.29\times10^4$ mol/m^3, $T = 300$ K, $\Delta t = 0.0005$, $\alpha = 0.0221$, $D = 10^{-14}$ m^2/s [94].

As can be seen from Fig. 1(c), the concentration profiles are similar at different time steps due to neglecting chemo-mechanical coupling and material softening effects. I.e, the concentration profile is constant in the core and shell but the magnitude changes, as it goes through a transition at the interface between the two regions, as seen in Fig. 1(c). The interface moves inward as lithiation proceeds. For the DISs, the conventional boundary condition for the radial stress is traction free at the free surface, which corresponds to the case $\tau^0 = 0$ and $K^s = 0$. In addition to the case for the conventional traction free boundary condition at the free surface, 6 different cases for $\tau^0 = \pm1$ N/m and $K^s = 0, \pm5$ N/m are investigated [30]. Both radial and hoop stresses have similar profiles as those in the conventional case ($\tau^0 = 0$ and $K^s = 0$), and only differ in magnitudes. For instance, when the residual surface stress is tensile ($\tau^0 = 1$ N/m), the radial and hoop stresses will be both in compression at the outer surface whereas when the residual surface stress (as shown in Fig. 1(a)–(b)) is compressive ($\tau^0 = -1$ N/m), the radial and hoop stresses will be both in tension at the free surface. When τ^0 is fixed, there is only a slightly difference, and the DIS decreases a little bit as K^s increases. To further understand the effects of the residual surface stress τ^0 and surface modulus K^s on the radial stress during ion insertion, the constitutive relation (Eq. (24)) for surface stress–strain may be revisited. The surface stress consists of two parts: the residual surface stress under unrestrained conditions and the diffusion induced stress due to surface elasticity. From Eq. (12), the maximum hoop surface strain occurs when full insertion is complete. In this case, the maximum value of $\varepsilon_{\theta\theta}^s$ is equal to α_s (α). For active materials undergoing relatively small volume variations, when τ^0 and K^s are of the same order of magnitude, $K^s\varepsilon_{\theta\theta}^s$ is much less than τ^0. As a result, τ^0 predominates the surface stress over K^s. To have a better picture of the influence of the surface modulus on the DISs, the radial and hoop stress profiles for a spherical $LiFePO_4$ particle with radius 5 nm at the time step 2000 Δt is given in Figure E.9. All the parameters are the same as in the 10 nm case except for the surface moduli ($\tau^0 = 2$ N/m and $K^s = 0, \pm10$ N/m) and interface thickness

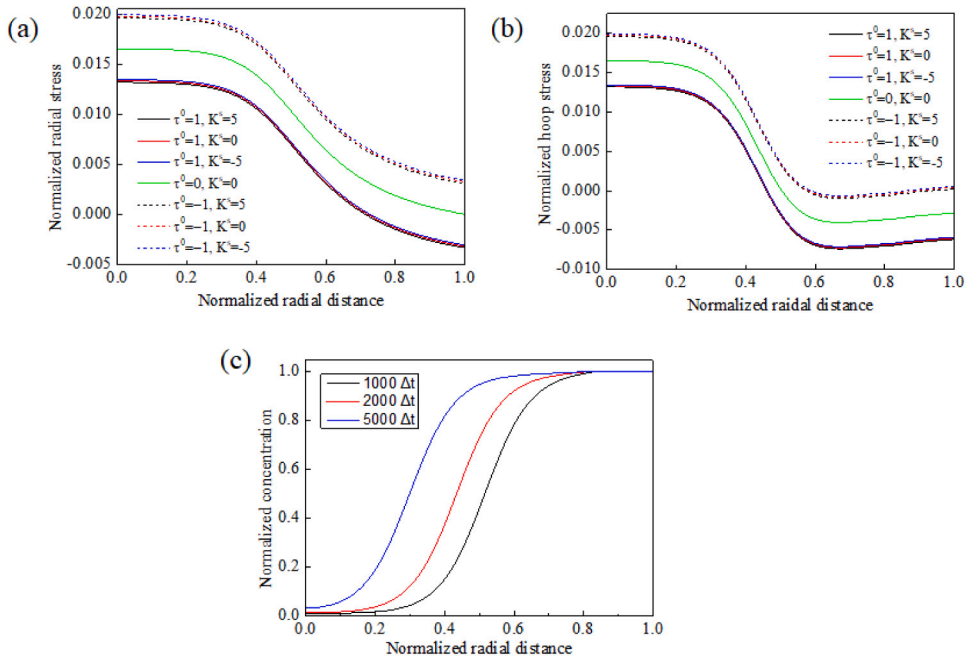

Fig. 1. (a) Normalized radial stress, and (b) hoop stress profiles at 2000 Δt with different surface elasticity parameters (residual surface stress τ^0 and surface modulus K^s, with units N/m) in a spherical $LiFePO_4$ particle of radius 10 nm. (c) Radial distribution of normalized concentration at 1000 Δt, 2000 Δt and 5000 Δt in the particle.

(2.5 nm). From the viewpoint that a tensile hoop stress is required for crack formation and propagation, the results immediately suggest that the residual surface tension may help avert crack growth during the lithium insertion process. The reason is that residual surface tension can convert the state of stress from tensile to compressive. As a result, the tendency to fracture can be reduced. To a lesser extent, by increasing the surface modulus, the radial and hoop stresses can decrease, making them less tensile or more compressive. This can be done by surface engineering of the particles.

2.1.2. DISs for elastic solids with surface elasticity only

To study the size effects, the DISs in spherical $LiFePO_4$ particles with different radii (ρ = 10, 20, 50, 100 nm) are studied. To make the study less complicated, first we consider surface elasticity only, i.e., l_ε = 0. The parameters are the same as in the previous parametric study except for κ^* = 0.0625, 0.015625, 0.0025, 0.000625, respectively, τ^0 = 1 N/m, and $K^s = 0$. The concentration distribution can be obtained by solving the weak form of Eq. (29). Then, the displacement field can be obtained by solving the weak form of the mechanical equilibrium Eq. (30). As a result, the stress evolution can be acquired by substituting the displacement field into the constitutive Eq. (31). The stress profiles and concentration distribution along the radial direction are plotted in Fig. 2:

It is evident from Fig. 2 that the concentration distribution is a step-like profile. Ion diffusion is "easier" in smaller particles, which in turn have a smooth interface between the lithiated and non-lithiated regions. Increasing, however, the particle radius results in a sharper interface. The DISs also have similar profiles; for the radial and hoop stresses, they remain constant in the core region (pristine part) and the radial stress equals the hoop stress for the same particle. The smaller the particle, the lower the stress it experiences. From the inner core towards the outer surface, there is a smooth transition in the radial stress from tensile to compressive while there is an abrupt change for the hoop stress across the interfaces. It can be also observed that when the radius is large enough, the boundary condition for the radial stress at the outer surface degenerates to the conventional stress-free one. Due to spherical symmetry, the hoop stress is equal to the radial stress in the core region. It is obvious that size effects exist, since the hoop stress in a 100 nm particle was 17.8% (0.0157) greater than that (0.01332) in a 10 nm particle. Brittle fracture is generally governed by the maximum tensile principal stress. Due to spherical symmetry, the tensile principal stress is equal to the radial/hoop stress in the core region. If the tensile principal stress is greater than a critical value, a crack may begin to nucleate. In this sense, particles with a smaller radius will have a more robust mechanical performance.

2.1.3. DISs for elastic solids with coupled surface elasticity and gradient elasticity

As can be seen from the above discussion, that size effects are prominent when the particle size is at the nanoscale. At such scales, the strain gradient cannot be neglected. The characteristic internal length (l_ε) in gradient models is normally much smaller than the macroscopic length scale. As a result it cannot be easily determined and obtained and it is often assumed that (l_ε) is a material constant that is related to the microstructure. It was estimated that for an atomic lattice: $l_\varepsilon = 0.25h$, where h is the lattice constant [95]. The lattice constant h can range from 10^{-8} m for some crystal lattices to 10^{-4} m for some granular materials [96]. Since the particles are all at the nanoscale, the characteristic internal length is chosen to be 2.5 nm. The other parameters are the same as in the case when considering surface elasticity only. To gain a better understanding of the influence of the strain gradient, a comparison between the two cases (with/without considering strain gradient effects) is performed. These two cases will be referred to as GradSEla (l_ε = 2.5 nm) and SEla (l_ε = 0), respectively. It is emphasized that both of these cases consider the surface elasticity terms, but GradSEla considers the gradient term as well. For dimensional consistency the gradient term is multiplied by an internal characteristic length (l_ε), and therefore setting it equal to zero dispenses with the gradient effect. Eq. (30) can be solved incrementally as shown in Appendix B. The stress profiles for particles with different radii of 10, 20, 50 and 100 nm are plotted in Fig. 3.

It can be recognized that there is a visible difference in DISs for smaller spherical $LiFePO_4$ particles. An interesting finding is that when strain gradient effects are considered, higher radial and hoop stresses are predicted compared to the surface elasticity case only. Considering that the DISs at the outer surface predicted with GradSEla might be

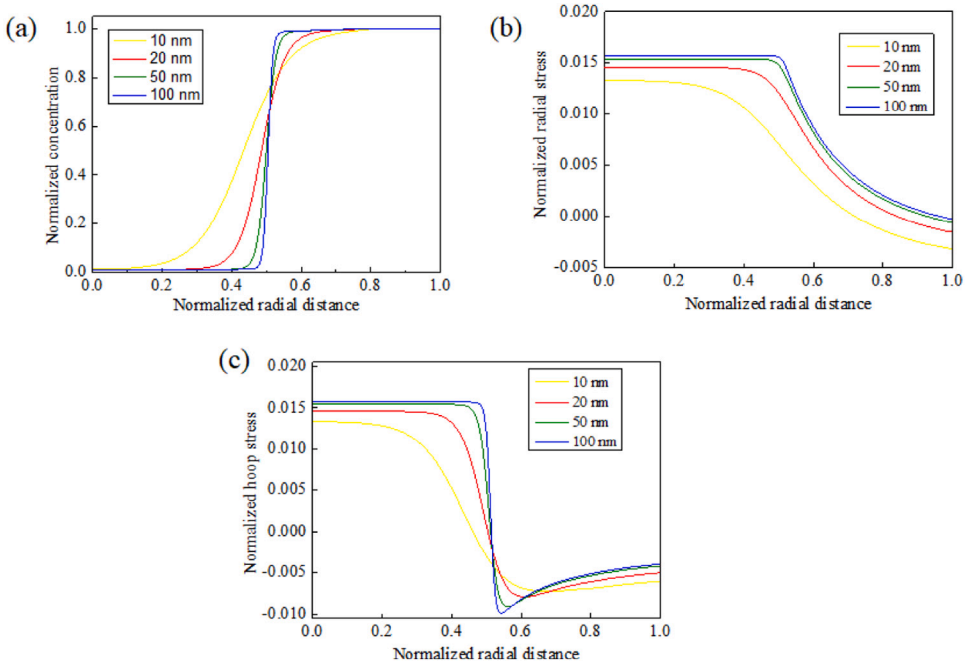

Fig. 2. Normalized radial distribution of (a) Normalized concentration, (b) Radial stress, and (c) hoop stress profiles in spherical $LiFePO_4$ particles with different radii (ρ = 10, 20, 50, 100 nm respectively) at 2000 Δt.

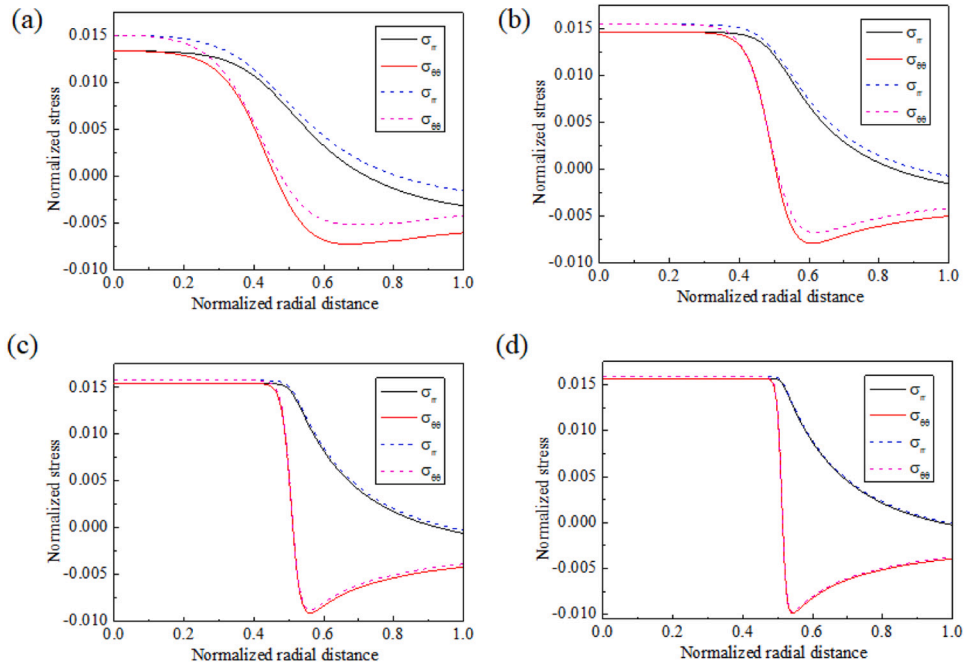

Fig. 3. Normalized stress profiles of a spherical $LiFePO_4$ particle with (a) 10 nm, (b) 20 nm, (c) 50 nm, and (d) 100 nm radius respectively when considering coupled surface elasticity with gradient elasticity (GradSEla) and surface elasticity (SEla) only at 2000 Δt. Solid line for SEla and dashed line for GradSEla.

quite different from those predicted with surface elasticity (SEla) only, it is important to take strain gradient effects into account especially for smaller particles. For larger particles (50 nm and 100 nm), the difference in stresses predicted between the two models is negligible. It should be clear from the considered examples that size effects are more obvious when the internal length is comparable to the particle size.

2.2. DISs under plastic deformation

The model does not take kinematic hardening and viscous effects into account, i.e. a quasi-static problem is solved. In the small deformation framework, the total strain $\boldsymbol{\varepsilon}$ can be additively decomposed into three parts: mechanical elastic strain $\boldsymbol{\varepsilon}^e$, chemically-induced elastic strain $\boldsymbol{\varepsilon}^c$ and plastic strain $\boldsymbol{\varepsilon}^p$:

$$\boldsymbol{\varepsilon} = \boldsymbol{\varepsilon}^e + \boldsymbol{\varepsilon}^c + \boldsymbol{\varepsilon}^p \tag{32}$$

For plasticity problems, it is better to use the rate form:

$$\dot{\boldsymbol{\varepsilon}} = \dot{\boldsymbol{\varepsilon}}^e + \dot{\boldsymbol{\varepsilon}}^c + \dot{\boldsymbol{\varepsilon}}^p \tag{33}$$

The lithiation-induced strain rate is:

$$\dot{\boldsymbol{\varepsilon}}^c = \alpha \dot{c}^* \mathbf{1} \tag{34}$$

α represents the expansion coefficient that results from the electro-chemical reaction. Hooke's law is given by:

$$\boldsymbol{\sigma} = \mathbb{C}^e : \boldsymbol{\varepsilon}^e = \mathbb{C}^e : (\boldsymbol{\varepsilon} - \boldsymbol{\varepsilon}^c - \boldsymbol{\varepsilon}^p) \tag{35}$$

where $\mathbb{C}^e$ is the elastic tensor $\mathbb{C}^e = \lambda\delta_{ij}\delta_{kl} + \Lambda\left(\delta_{ik}\delta_{jl} + \delta_{il}\delta_{jk}\right)$, and λ and Λ are Lamé constants. Hooke's law in rate form is:

$$\dot{\boldsymbol{\sigma}} = \mathbb{C}^e : (\dot{\boldsymbol{\varepsilon}} - \dot{\boldsymbol{\varepsilon}}^p) + \boldsymbol{N}\dot{c} \tag{36}$$

where $\boldsymbol{N}$ is the coupling matrix accounting for deformations induced by changes in the chemical composition. For a linear elastic and isotropic material, it is given by:

$$\boldsymbol{N} = -3\alpha K \mathbf{1} \tag{37}$$

where $K = \left(\lambda + \frac{2}{3}\Lambda\right)$ is the bulk modulus. For the sake of simplicity, we consider von Mises J_2 plasticity with isotropic hardening. The first theory of plasticity which incorporated effects of gradients of plastic strain was that introduced by Aifantis [61]. Strain gradient theories consider the gradient of the plastic strain as an independent variable, and in doing so it is required to introduce a length scale parameter (similar as in gradient elasticity). The energy contribution due to plastic deformation within the gradient framework is given by:

$$\psi^p(\zeta, \nabla\zeta) = \frac{1}{2}H\zeta^2 + \sigma_y^0\zeta + \frac{1}{2}\beta {l_p}^2 |\nabla\zeta|^2 \tag{38}$$

where ζ is a strain-like internal variable (normally equivalent to the plastic strain), H is the linear isotropic hardening modulus, β is the hardening modulus related to the plastic strain gradient, σ_y^0 is the initial yield stress and l_p is the internal length scale. The weak form of the governing equation can be given as:

$$\int_{\Omega^p} \frac{\partial f}{\partial \boldsymbol{\sigma}} : \mathbb{C}^e : \dot{\boldsymbol{\varepsilon}}\delta\dot{\gamma} dV - \int_{\Omega^p}\left(2\Lambda + \frac{2}{3}H\right)\dot{\gamma}\delta\dot{\gamma} dV - \int_{\Omega^p}\frac{2}{3}\beta {l_p}^2 \nabla\dot{\gamma}\cdot(\nabla\delta\dot{\gamma})\, dV = 0 \tag{39}$$

where f is the yield function, $\dot{\gamma}$ is the rate of the plastic multiplier, $\delta\dot{\gamma}$ is an arbitrary test function, and Ω^p is the plastic domain. Details are given in Appendix C.

When plasticity is taken into consideration, the constitutive relations for a spherical particle can be given by:

$$\left.\begin{aligned} \sigma_{rr} &= \frac{E}{(1+\upsilon)(1-2\upsilon)}\left[(1-\upsilon)\left(\frac{du}{dr} - \varepsilon_{rr}^p - \alpha c^*\right) + 2\upsilon\left(\frac{u}{r} - \varepsilon_{\theta\theta}^p - \alpha c^*\right)\right] \\ \sigma_{\theta\theta} &= \frac{E}{(1+\upsilon)(1-2\upsilon)}\left[\left(\frac{u}{r} - \varepsilon_{\theta\theta}^p - \alpha c^*\right) + \upsilon\left(\frac{du}{dr} - \varepsilon_{rr}^p - \alpha c^*\right)\right] \end{aligned}\right\} \tag{40}$$

where ε_{rr}^p and $\varepsilon_{\theta\theta}^p$ are the plastic strain components. And the deviatoric parts are:

$$\sigma_{rr}' = \frac{2}{3}\left(\sigma_{rr} - \sigma_{\theta\theta}\right), \sigma_{\theta\theta}' = \sigma_{\phi\phi}' = -\frac{1}{3}\left(\sigma_{rr} - \sigma_{\theta\theta}\right) \tag{41}$$

The rates of the plastic strain components are given by:

$$\dot{\varepsilon}_r^p = \dot{\gamma}\frac{\sigma_{rr}'}{\|s\|},\ \dot{\varepsilon}_\theta^p = \dot{\gamma}\frac{\sigma_{\theta\theta}'}{\|s\|} \tag{42}$$

For the associative flow rule,

$$\frac{\partial f}{\partial \boldsymbol{\sigma}} = \mathrm{sign}(\sigma_{rr}')\frac{1}{\sqrt{6}}\mathrm{diag}\,(2,-1,-1) \tag{43}$$

$$\frac{\partial f}{\partial \boldsymbol{\sigma}} : \mathbb{C}^e : \dot{\boldsymbol{\varepsilon}} = \frac{4\Lambda}{\sqrt{6}}\left(\frac{\partial \dot{u}}{\partial r} - \frac{\dot{u}}{r}\right)\mathrm{sign}(\sigma_{rr}') \tag{44}$$

The mechanical equilibrium equation can be solved in its variational form as:

$$2\rho\sigma_{\theta\theta}^s(\delta u)\Big|_{r=\rho} + \int_0^\rho\left(\sigma_{rr}\frac{\partial(\delta u)}{\partial r} + 2\sigma_{\theta\theta}\frac{\delta u}{r}\right)r^2 dr = 0 \tag{45}$$

The framework for surface elasticity in plasticity, is essentially the same as in the elastic case presented previously. The finite element solution procedures are given in Appendix D.

2.2.1. Parametric study of surface elasticity for elasto-plastic materials

Silicon is an attractive anode material for lithium ion batteries due to being able to provide the highest known capacity upon lithiation. Herein, therefore, a Si anode is analyzed. Cracks have been observed by many experiments during the first lithiation process of spherical Si/Sn electrode particles [3,6,10]. Plastic deformation, therefore, must have occurred since the purely elastic model predicts a comprehensive hoop stress on the outer surface, which prohibit crack propagation and is believed to be the cause of experimentally observed cracks during the lithiation process. Many experiments have verified that crystalline Si (c-Si) undergoes phase separation during the lithiation process and the thickness of the phase boundary, which separates the Li-rich and Li-poor phases, was observed to be about 1 nm [10,11,97–100] in c-Si electrodes. As explained earlier in Section 2.1.1, depending on the material, the surface elastic constants can be either positive or negative. To study the effects of these parameters, the DISs of a spherical particle with 10 nm radius ($\rho = 10$ nm) are analyzed. As mentioned the interface thickness is assumed to be 1 nm. The parameters for silicon are taken according to the literature as follows: $E = 90$ GPa, $\upsilon = 0.24$, $M^* = 1$, $i^* = 1$, $\sigma_y^0 = 0.01E$, $H_0 = \pm 0.01E$, $\kappa^* = 0.04$, $\Xi = 1.2 \times 10^{-5}$ m^3/mol, $c_{\max} = 3.67 \times 10^5$ mol/m^3, $T = 300$ K, $\Delta t = 0.0005$, $\alpha = 0.6$ [52]. As in Section 2.1.1, 6 different sets of surface elastic constants ($\tau^0 = \pm 1$ N/m and $K^s = 0, \pm 5$ N/m [30]) are investigated in addition to the conventional case ($\tau^0 = 0$ and $K^s = 0$). Since the chemo-mechanical coupling effect is neglected, the concentration profiles at $1000\Delta t$, $2000\Delta t$ and $5000\Delta t$ are as shown in Fig. 4(a). The concentration profiles at different time steps are very similar to each other. As lithiation proceeds, the phase interface moves towards the center of the particles. The radial distribution of the normalized radial stress is as shown in Fig. 4(b). The conventional traction-free boundary condition requires that the radial stress vanishes at the outer surface. This is the case when $\tau^0 = 0$ and $K^s = 0$. However, depending on the values of the surface elastic constants, the radial stress at the outer surface can be either in compression ($\tau^0 = \pm 1$ N/m, $K^s = 5$ N/m, or $\tau^0 = 1$ N/m, $K^s = 0$) or in tension ($\tau^0 = \pm 1$ N/m, $K^s = -5$ N/m, or $\tau^0 = -1$ N/m, $K^s = 0$). The radial distribution of the normalized hoop stress is as shown in Fig. 4(c). In most cases, the hoop stress at the outer surface is tensile except when $\tau^0 = 1$ N/m and $K^s = 5$ N/m. It can be seen that the hoop stress on the outer surface is maximum when the surface elastic constants are negative ($\tau^0 = -1$ N/m and $K^s = -5$ N/m) and minimum when the surface elastic constants are positive ($\tau^0 = 1$ N/m and $K^s = 5$ N/m). The stresses for different surface elastic constants have similar profiles. As for the radial distribution of the normalized von Mises stress (Fig. 4(d)) and equivalent plastic strain (Fig. 4(e)), they have the same profiles for different surface parameters. This means the surface parameters can affect the stress state of the radial and hoop stresses on the outer surface, but not the von Mises stress and equivalent plastic strain distribution. To further understand the effects of residual surface stress τ^0 and surface modulus K^s on the hoop stress during ion insertion, the constitutive relation (Eq. (24)) for the surface stress–strain and the mechanical equilibrium condition (Eq. (A.7)) are revisited. The surface stress comprises of two parts: the residual surface stress under unrestrained conditions and the diffusion induced stress due to surface elasticity. From Eq. (12), the maximum hoop surface strain occurs when full insertion is complete. In this case, the maximum value of $\varepsilon_{\theta\theta}^s$ is equal to α_s (α). For electrode materials undergoing huge volume changes, when τ^0 and K^s are of the same order of magnitude,

$K^s\varepsilon^s_{\theta\theta}$ is about the same order of τ^0. As a result, the surface stress relies on both τ^0 and K^s. In our case, when $K^s = 0, \pm 5$ N/m, $K^s\varepsilon^s_{\theta\theta}$ is approximately 0, ± 3 N/m respectively. That is the reason why some combinations of τ^0 and K^s lead to a compressive radial stress and others lead to a tensile radial stress at the surface. As for the hoop stress at the surface, according to the mechanical equilibrium condition (Eq. (A.7)), $\sigma_{\theta\theta}\Big|_{r=\rho} = \frac{\rho}{2}\frac{\partial \sigma_{rr}}{\partial r}\Big|_{r=\rho} + \sigma_{rr}\Big|_{r=\rho}$. This means that the hoop stress at the surface does not only depend on the radial stress at the surface but also relies on the rate of change of the radial stress at the surface with respect to its position. The latter corresponds to the slope of Fig. 4(b) at the surface, which is always positive. This means that by tuning the values of τ^0 and K^s, the hoop stress at the surface can be reduced. It is even possible to change the stress state of the hoop stress at the surface from tension to compression. To have a better understanding of the influence of the surface modulus on the DISs, the radial and hoop stress profiles for a spherical Si particle with radius 5 nm at the time step 2000 Δt is given in Figure E.10. All the parameters are the same as in the 10 nm case except for the surface moduli. The results suggest that when the residual surface stress and surface elastic constants are sufficiently large, the hoop stress on the outer surface may become compressive, which can hinder crack growth during ion-insertion.

In [101], it was found that the structural stability of Si anodes can be significantly enhanced by introducing a nanoporosity on the surface of micropyramid patterned Si anodes. No fracture was observed in the porous patterned pyramids under either high or low current densities, however, severe fracture occurred (without the surface porosity) at low current densities. The model presented here can help explain this phenomenon. The surface elastic constants do not depend on the bulk size but are strongly dependent on the surface morphology and orientation, while the surface stress is closely related to the surface states [102]. This means that surface modification can be an effective approach to improving the mechanical stability of high-capacity electrodes. Our work herein, shows that, surface elasticity is appropriate to interpret the results of [101].

2.2.2. DISs for elasto-plastic materials with surface elasticity only

In this section, the DISs in spherical Si electrode particles with different radii are considered and surface effects are taken into consideration. The parameters used in the simulation are the same as in Section 2.2.1 except $\tau^0 = 1$ N/m and $K^s = 0$. Spherical silicon electrode particles with radii of 10 nm, 20 nm, 50 nm and 100 nm are analyzed; according to Table 1 the corresponding $\kappa^* = 0.04, 0.01, 0.0025, 0.0004$, respectively. For the case where neither chemo-mechanical coupling nor material softening are considered, the concentration evolution is shown in Fig. 5(a). Fig. 5(b)–(e) shows the DIS profiles and plastic strain distribution at 2000 Δt when only surface effects are taken into account without the gradient of the plastic strain being considered.

At the initial stages, the Si electrode undergoes elastic deformation and the DIS profiles are similar to those in the elastic case. However, due to the large volume expansion during lithiation, yielding and plastic deformation occurs. An interesting observation is that a stress state transition takes place after the onset of plasticity. The radial and hoop stresses in the core region remain constant. In the elastic case (Fig. 2(b–c)), the core region is in tension while in the plastic case, it undergoes compression. The hoop stress at the outer surface, is in compression for the elastic case (Fig. 2(c)), while for the plastic case (Fig. 5(b)), it transits from compression to tension, and therefore fracture will always initiate without the possibility of surface modification to prevent it, as was in the previous GradSEla and SEla cases in Section 2.1.2 and Section 2.1.3. It can be recognized that the radial stress at the outer surface degenerates to the traction-free one when the particle size is large enough (greater than 50 nm). The von Mises stresses (Fig. 5(c)) gradually increase from the core towards the shell, and as soon as they exceed the yield stress, plastic deformation begins to take place. As a result, there is no plastic deformation taking place near the core region. As lithiation progresses, the phase interface moves from the exterior shell towards the center. The profiles for the von Mises stress and plastic strain are very similar, and the difference lies in their magnitude. The smaller particles undergo much lower stresses (Fig. 5(c) and plastic deformation (Fig. 5(d) than the larger ones. Smaller particles also experience a relatively lower hoop stress at the outer surface. The size effect is prominent for smaller particles and the hoop stress at the outer surface can be decreased greatly when the particle size decreases.

2.2.3. DISs or elasto-plastic materials with coupled surface elasticity and gradient plasticity

As it was mentioned earlier, the strain gradient effects cannot be neglected at the nanoscale. For plastic deformation, plastic strain is dominant, and therefore the plastic strain gradient should be taken into account. The characteristic length (l_p) can be related to the plastic zone size (r_p). From Irwin's approximation, it can be given by:

$$r_p = \frac{1}{3\pi}\left(\frac{K_{I_c}}{\sigma^0_y}\right)^2 \tag{46}$$

where K_{I_c} is the fracture toughness of the material. According to [103], the characteristic length (l_p) was chosen to be $0.03r_p$. It is assumed that $K_{I_c} = 4.62$ MPa $\sqrt{\text{m}}$ [55] and $\sigma^0_y = 0.01E = 9$ GPa, $l_p = 0.03r_p = 2$ nm, while the other parameters were kept the same as in the previous section for spherical Si particles. By solving the weak form of Eq. (C.16), the plastic multiplier γ can be obtained. Then by solving Eq. (44), the displacement field $\boldsymbol{u}$ can be obtained, which when substituted into the constitutive Eq. (40), allows to obtain the DISs. The cumulative plastic strain is plotted by the incremental form of Eq. (C.10). The DISs and plastic strain profiles are plotted in Fig. 6.

The radial stress (Fig. 6(a)) and equivalent plastic strain in the spherical Si electrode particles (Fig. 6(d)) have similar distributions as the case when only surface elasticity (Fig. 5(a) and (d)) was considered. An interesting finding is that there are slight oscillations in both the hoop stress (Fig. 6(b)) and von Mises stress (Fig. 6(c)) profiles. In particular, for particles with 10 nm and 20 nm radii, the local maxima of the hoop stress are located somewhere close to their outer surfaces but not exactly on the outer surface. This is consistent with the fact that experiments have shown that cracks initiate at the outer surface of Si and Sn particles during complete Li-ion insertion [3,10]. To better picture the differences, the DIS profiles of these two cases are depicted in Fig. 7. The two cases (with/without plastic strain gradient effect) are referred to as GradSPla ($l_p = 2$ nm) and SPla ($l_p = 0$) respectively. It is noted that both cases consider surface elastic terms, and the model with no gradient effects is deduced by setting the internal length parameter (since it is multiplied with the plastic strain gradient) equal to zero.

As can be seen from the plots (Fig. 7), size effects are distinct for smaller particles. An interesting observation is that higher radial and hoop stresses are predicted when the plastic strain gradient was considered. For the von Mises stress, the coupled surface elasticity with strain gradient model (GradSEla) predicted a lower von Mises stress than the models with surface elasticity (SEla) only. Whereas the coupled surface elasticity with plastic strain gradient models (GradSPla) predicted a higher von Mises stress than the models using surface elasticity within classical plasticity (SPla) only. As the particle size increased, the two results (i.e, with and without gradient effect) became close to each other. In both, the GradSPla and the SPla models, the maxima in the hoop stress occurred near the surface. Since the tensile hoop stress promotes mode-1 fracture, cracks are likely to initiate from the outer surface. The DIS comparisons at 1000 Δt and 5000 Δt have similar trends. For particles that undergo plastic deformation, another quantity of interest is the equivalent plastic strain. The comparisons of the two models (SPla vs. GradSPla) are plotted in Fig. 8.

It is obvious that the two models gave similar equivalent plastic strain profiles, with gradient models predicting a slightly lower plastic deformation. It is found that the core region remained elastic during lithiation since the equivalent plastic strain was 0. This was attributed

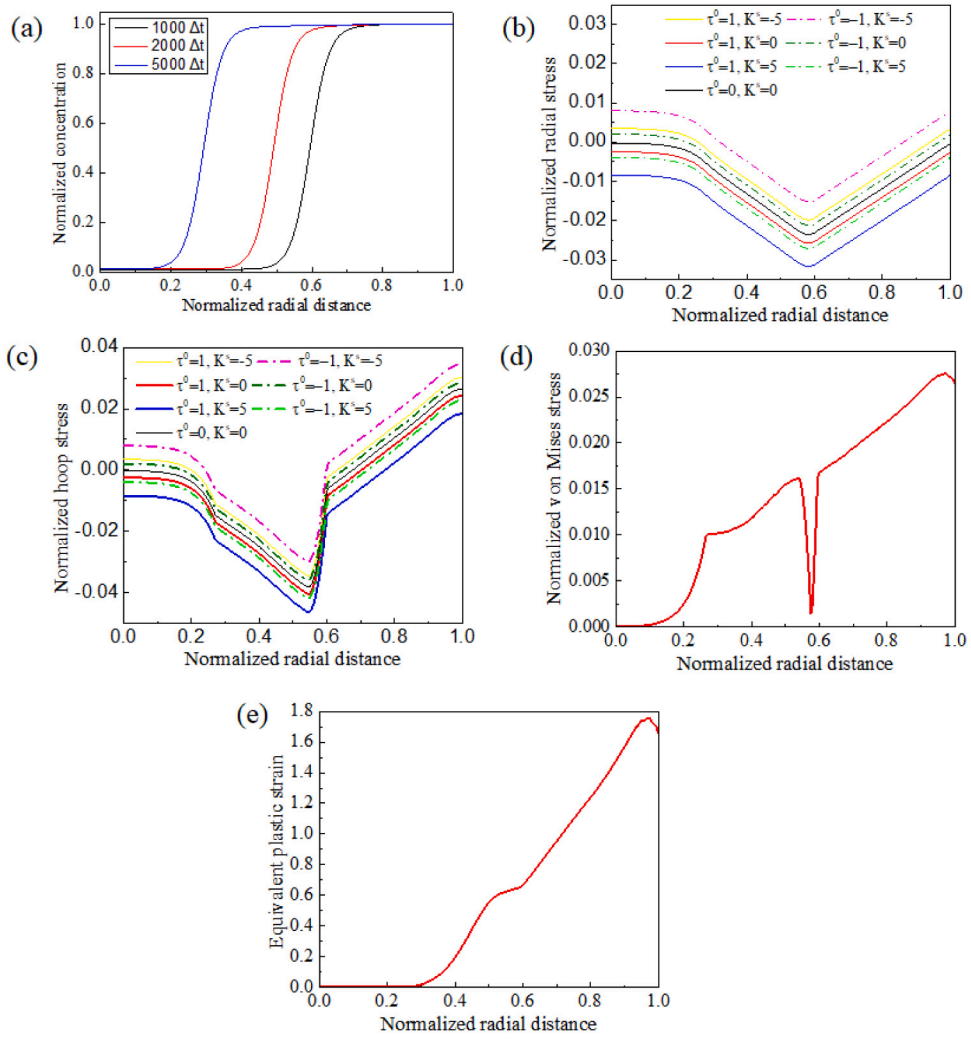

Fig. 4. (a) Radial distribution of normalized concentration at 1000 Δt, 2000 Δt and 5000 Δt in a spherical Si electrode of radius 10 nm. (b) Normalized radial stress, (c) normalized hoop stress, (d) Normalized von Mises stress, and (e) equivalent plastic strain profiles at 2000 Δt with surface elasticity parameters (residual surface stress τ^0 and surface modulus K^s, with units N/m) in the electrode.

to the fact that the particle underwent phase segregation. As lithiation proceeded, the phase boundary interface kept moving inward. The outer part of the particle yielded first while the concentration of the core remained unaltered. As a result, no plastic deformation was anticipated for the core region. As the interface between the lithiated/non-lithiated regions kept propagating, the equivalent plastic strain accumulated, and more material deformed plastically. For both cases (GradSPla and SPla), the distribution of the equivalent plastic strain in larger particles near the interface was steeper since the concentration profile was sharper, while for the smaller particles it was relatively smoother. The maximum equivalent plastic strains for the GradSPla case at 5000 Δt are 2.03, 2.28, 2.49, and 2.56 respectively. For ductile fracture, if we assume damage initiates once the equivalent plastic strain exceeds a critical value, again we can see that smaller particles have a better mechanical performance.

3. Conclusions

Many experiments have shown that electrode materials display strong size effects when their dimensions are reduced down to the nano-scale. Classical mechanics theories do not include a characteristic length and cannot explain these size effects. Size effects can be efficiently captured through gradient theories and theories that capture surface effects. Furthermore, for electrode particles undergoing phase transformations, the stress/strains vary sharply across the thin interface, and in such cases, the gradient effects are significant and cannot be neglected.An additional aspect that needs to be accounted for in modelling electrodes, are surface effects, since the surface area to volume ratio increases as the bulk size decreases. In the present work, both effects were considered by incorporating surface elasticity in gradient models.

Due to the presence of surface effects, the stress on the outer surface can be significantly reduced. In this work it was shown that the surface modulus affects the stress state, and under some circumstances, it is even possible to change the stress state from tension to compression. For elastic electrode particles, when the residual surface stress is tensile, the hoop stress at the outer surface is compressive. For elasto-plastic electrodes, when the residual surface stress and the surface elastic modulus are both positive, the hoop stress at the outer surface remains compressive. Since a compressive hoop stress prevents cracks from propagating, this suggests that surface modification could be an effective approach to improving the structural integrity of electrodes during the lithiation process. This is in agreement with experimental results which show that inducing a porosity on the surface of electrode particles drastically improves their mechanical integrity during cycling. However, systematic experiments must be done in order to understand how the surface morphology can affect the value of the surface modulus, and hence improve the mechanical stability based on the model predictions.

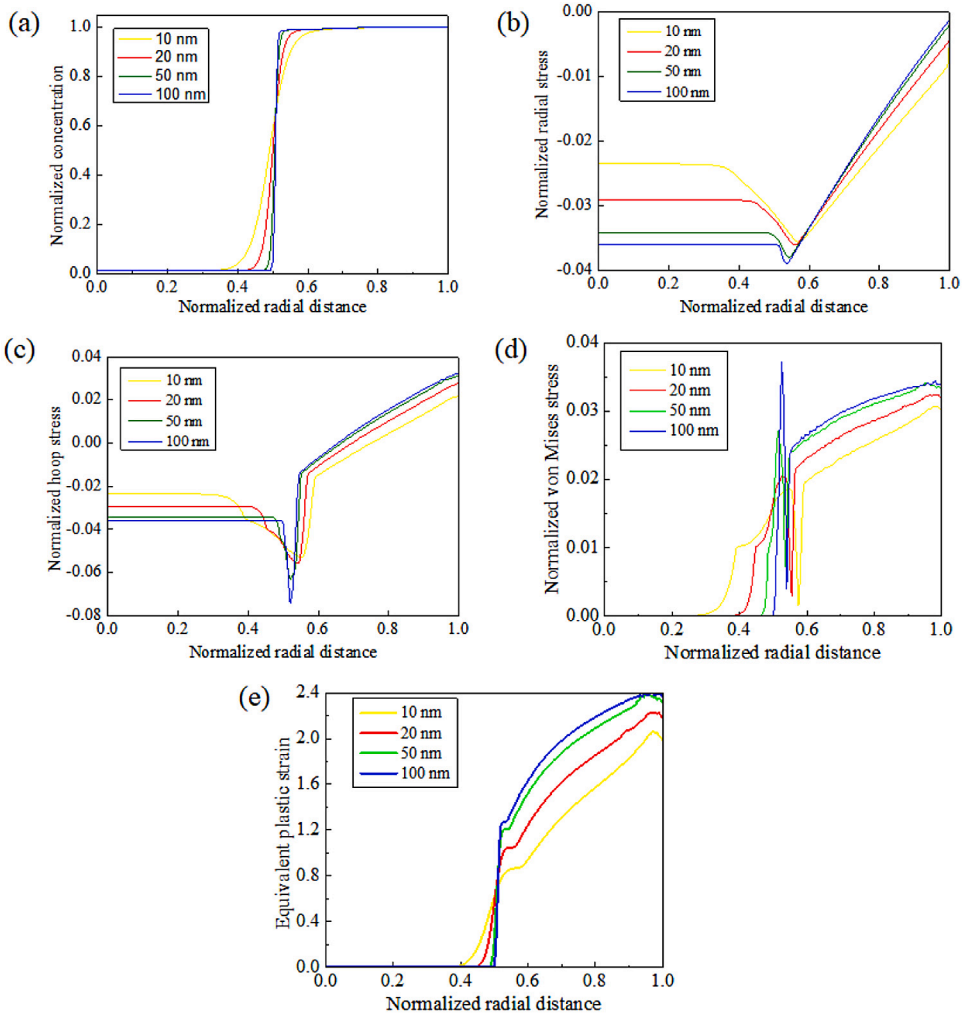

Fig. 5. Radial distribution of (a) normalized concentration, (b) normalized radial stress, (c) normalized hoop stress, (d) normalized von Mises stress and (e) equivalent plastic strain profiles of spherical Si electrode particles with different radii (ρ = 10, 20, 50, 100 nm respectively) at 2000 Δt when considering surface effect only.

When strain gradient effects are considered, slightly higher radial and hoop stresses are predicted for both elastic deformation and plastic deformation. In the plastic case higher von Mises stresses but lower equivalent plastic strains are predicted. It is shown that smaller particles have a better mechanical performance. It can therefore be seen that to better understand the DISs in a nano particle, both surface effects and gradient effects cannot be neglected. These findings render prospective insights for designing next-generation mechanically stable electrode materials that undergo phase transformations.

CRediT authorship contribution statement

Bo Wang: Investigation, Writing – original draft, Software. **Katerina E. Aifantis:** Methodology, Writing – original draft, Validation, Supervision.

Declaration of competing interest

The authors declare that they have no known competing financial interests or personal relationships that could have appeared to influence the work reported in this paper.

Acknowledgment

The authors are grateful to the National Science Foundation, United States for supporting this work through the CMMI grant (CMMI-1762602).

Appendix A. Derivation of the weak form of the governing equation within strain gradient elasticity framework

Define the effective stress tensor as:

$$\boldsymbol{\sigma}^e = \boldsymbol{\sigma}^c - \nabla \cdot \boldsymbol{\tau} \tag{A.1}$$

It can be expressed as:

$$\boldsymbol{\sigma}^e = \boldsymbol{\sigma}^c - l_\varepsilon{}^2 \nabla^2 \boldsymbol{\sigma}^c \tag{A.2}$$

For isotropic and homogeneous materials under dilatational deformation due to Li de-insertion, the constitutive relations for classical mechanics can be expressed by:

$$\sigma^c = \lambda \mathrm{tr}\,(\varepsilon)\,\mathbf{1} + 2\Lambda\varepsilon - (3\lambda + 2\Lambda)\,\alpha c^* \mathbf{1} \tag{A.3}$$

This is the non-gradient part of the stress. When no body force is present, the mechanical equilibrium condition (balance of momentum for the mechanical stress) is given by:

$$\nabla \cdot \boldsymbol{\sigma}^e = \mathbf{0} \tag{A.4}$$

Because of the symmetry of the spherical particle, all the shear stresses are zero, indicating that σ^c_{rr} and $\sigma^c_{\theta\theta}$ are principal stresses.

Considering a spherical particle during the lithiation process, the non-gradient strain and stress tensors are given by $\boldsymbol{\varepsilon} = \mathrm{diag}\left(\frac{\partial u}{\partial r}, \frac{u}{r}, \frac{u}{r}\right)$ and $\boldsymbol{\sigma}^c = \mathrm{diag}\left(\sigma^c_{rr}, \sigma^c_{\theta\theta}, \sigma^c_{\theta\theta}\right)$ where u is the radial displacement, σ^c_{rr} is the

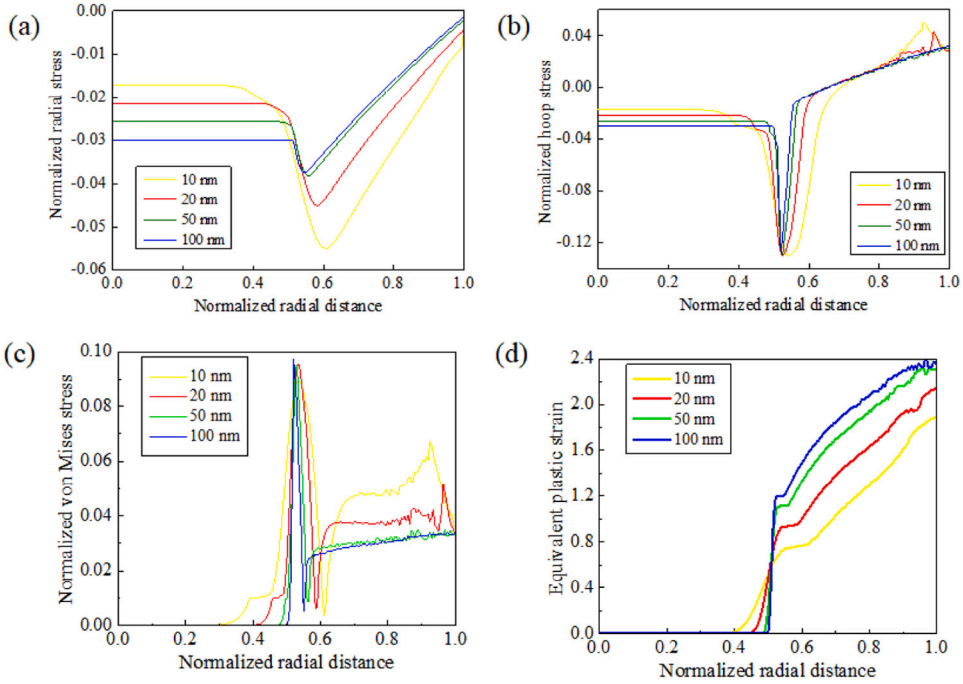

Fig. 6. Radial distribution of (a) normalized radial stress, (b) normalized hoop stress, (c) normalized von Mises stress and (d) equivalent plastic strain profiles of spherical Si electrode particles with different radii (ρ = 5, 10, 20, 50, 100 nm respectively) at 2000 Δt when considering both surface effect and plastic strain gradient effect.

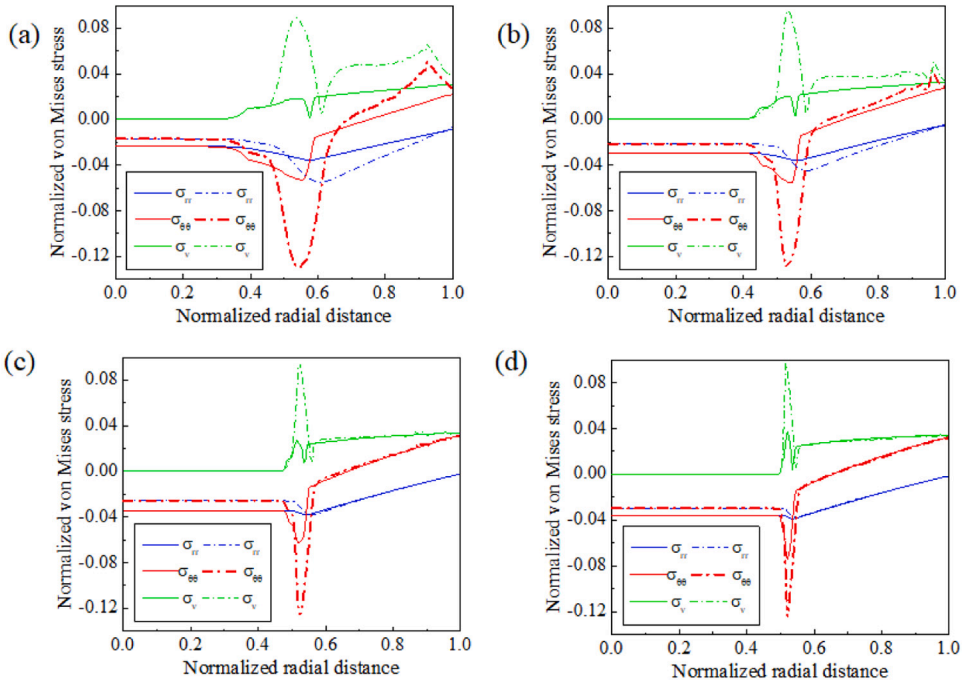

Fig. 7. Normalized stress profiles of a spherical Si particle with (a) 10 nm, (b) 20 nm, (c) 50 nm, and (d) 100 nm radius respectively when considering coupled surface elasticity with gradient plasticity (GradSPla) and surface elasticity (SPla) only at 2000 Δt. Solid for SPla and dash for GradSPla.

non-gradient radial stress and $\sigma^c_{\theta\theta}$ is the non-gradient hoop (tangential) stress. The divergence of the effective stress tensor is:

$$\nabla \cdot \boldsymbol{\sigma}^e = \left[\frac{\partial \sigma^e_{rr}}{\partial r} + \frac{2\left(\sigma^e_{rr} - \sigma^e_{\theta\theta}\right)}{r}, 0, 0 \right]^T \tag{A.5}$$

The Laplacian of the non-gradient stress tensor is:

$$\nabla^2 \boldsymbol{\sigma}^c = \operatorname{diag}\left(\frac{\partial}{\partial r}\left(\frac{\partial \sigma^c_{rr}}{\partial r} + \frac{2\left(\sigma^c_{rr} - \sigma^c_{\theta\theta}\right)}{r} \right), \frac{1}{r}\left(\frac{\partial \sigma^c_{rr}}{\partial r} + \frac{2\left(\sigma^c_{rr} - \sigma^c_{\theta\theta}\right)}{r} \right), \right.$$

$$\left. \frac{1}{r}\left(\frac{\partial \sigma^c_{rr}}{\partial r} + \frac{2\left(\sigma^c_{rr} - \sigma^c_{\theta\theta}\right)}{r} \right) \right) \tag{A.6}$$

The mechanical equilibrium equation now becomes:

$$\frac{\partial \sigma^e_{rr}}{\partial r} + \frac{2\left(\sigma^e_{rr} - \sigma^e_{\theta\theta}\right)}{r} = 0 \tag{A.7}$$

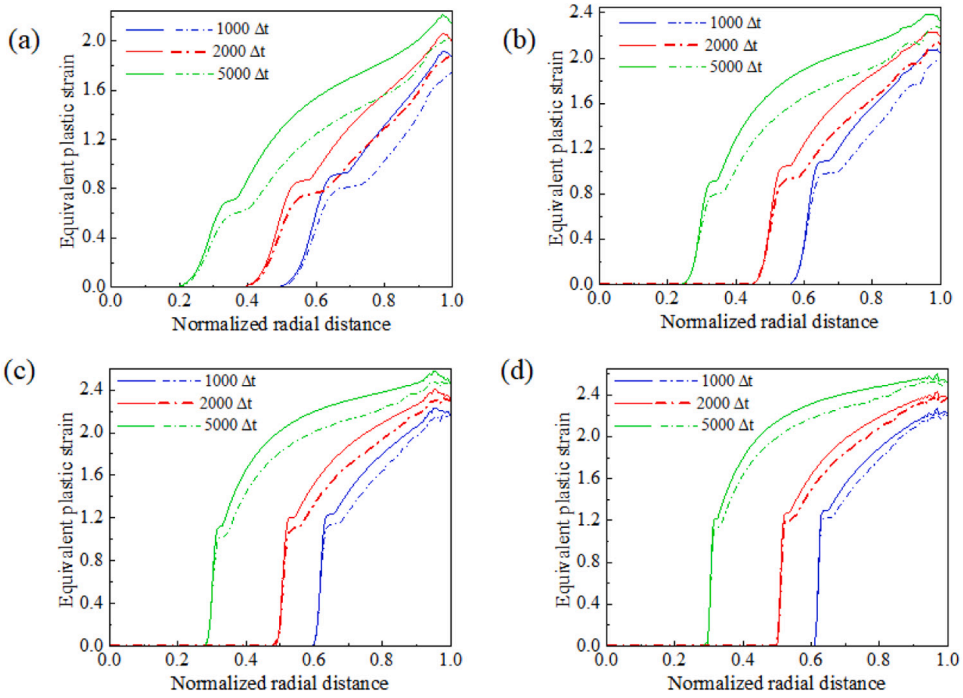

Fig. 8. Radial distributions of equivalent plastic strain of a spherical particle with (a) 10 nm, (b) 20 nm, (c) 50 nm, and (d) 100 nm radius respectively when considering coupled surface elasticity with gradient plasticity (GradSPla) and surface elasticity (SPla) only at different time stages (1000 Δt, 2000 Δt and 5000 Δt. Solid for SPla and dash for GradSPla.

The weak form of the mechanical equilibrium equations can be given by:

$$\int_0^{\rho} \delta u \left(\frac{\partial \sigma_{rr}^e}{\partial r} + \frac{2\left(\sigma_{rr}^e - \sigma_{\theta\theta}^e\right)}{r} \right) r^2 dr = 0 \tag{A.8}$$

where δu is a test function. The boundary conditions for this problem are: zero radial displacement at the center of the sphere and the radial stress must satisfy the mechanical equilibrium on the outer surface of the spherical particle, i.e., $u\big|_{r=0} = 0$, $\sigma_{rr}^e\big|_{r=\rho} = -\frac{2\sigma_{\theta\theta}^s}{\rho}$. For large particles, $\frac{2\sigma_{\theta\theta}^s}{\rho} \to 0$, which is the conventional traction-free boundary condition at the outer surface. The variationally consistent condition for the higher order stress is given by:

$$l_\varepsilon{}^2 \left(\frac{\partial \sigma_{rr}^c}{\partial r} + \frac{2\left(\sigma_{rr}^c - \sigma_{\theta\theta}^c\right)}{r} \right)\Big|_{r=\rho} = 0 \tag{A.9}$$

Integrating the weak form of the mechanical equilibrium equation by parts and applying boundary conditions, one can obtain:

$$\begin{aligned} &-\int_0^{\rho} \delta u \left(\frac{\partial \sigma_{rr}^e}{\partial r} + \frac{2\left(\sigma_{rr}^e - \sigma_{\theta\theta}^e\right)}{r} \right) r^2 dr \\ &= 2\rho\sigma_{\theta\theta}^s (\delta u)\big|_{r=\rho} + \int_0^{\rho} \left(\sigma_{rr}^c \frac{\partial (\delta u)}{\partial r} + 2\sigma_{\theta\theta}^c \frac{\delta u}{r} \right) r^2 dr \\ &+ \int_0^{\rho} l_\varepsilon{}^2 \left(\frac{\partial \sigma_{rr}^c}{\partial r} + \frac{2\left(\sigma_{rr}^c - \sigma_{\theta\theta}^c\right)}{r} \right) \left(\frac{\partial^2 (\delta u)}{\partial r^2} r^2 + 2r \frac{\partial (\delta u)}{\partial r} - 2(\delta u) \right) dr \end{aligned} \tag{A.10}$$

Appendix B. Numerical implementation of the model for elastic solids

In order to seek the solutions, the finite element method is used. Due to spherical symmetry, the problem can be reduced to a one-dimensional problem. The weak form cannot be solved directly. Instead, we have to discretize in both the temporal and spacial space. Therefore, Eq. (29) can be rewritten as:

$$\int_\Omega \frac{{c_{n+1}}^* - {c_n}^*}{\Delta t_n} v dr = -\int_{\partial\Omega} iv dS - \int_\Omega M {c_n}^* \left(1 - {c_n}^*\right) \nabla \mu_n \nabla v dr \tag{B.1}$$

$$\begin{aligned} \int_\Omega \mu_{n+1} w dV = &\int_\Omega RT \left[4a_0 \left({c_n}^* - \frac{1}{2} \right)^3 + 2a_1 \left({c_n}^* - \frac{1}{2} \right) \right] w dV \\ &- \int_\Omega \kappa c_{\max} \nabla {c_n}^* \nabla w dV \end{aligned} \tag{B.2}$$

where the subscripts $n+1$ and n are the corresponding values at the time step t_{n+1} and t_n respectively, with $\Delta t_n = t_{n+1} - t_n$ being the n^{th} time step. By substituting Eq. (31) into Eq. (A.10), we have the weak form in terms of the displacement. By using this kind of mixed formulation, the problem reduces to finding ${c_{n+1}}^*$ and μ_{n+1} given that ${c_n}^*$ and μ_n are known. The built-in DOLFIN Newton solver in FEniCS [104] is used to solve the nonlinear equations. As for the mechanical equilibrium equation, the built-in NonlinearVariationalSolver in FEniCS is employed. The basic idea is to calculate the Gateaux derivative of the nonlinear form $F(u; q) = 0$ (corresponding to Eq. (A.10)). Thus, the Jacobian and the trial function will be automatically computed and solved. By solving the diffusion equation (Eqs. (B.1) and (B.2)), the concentration and the chemical potential can be obtained. Then the radial displacement can be obtained by solving the weak form of the mechanical equilibrium equation (Eq. (A.10)). The unknown field variables (c^*, μ, u) can be solved by using this staggered scheme at every time step.

Appendix C. Derivation of the weak form of the governing equation within strain gradient plasticity framework

The effective yield stress Σ, can be defined as the variational derivative of the total plastic energy with respect to the effective plastic strain. The variation of the plastic energy is

$$\delta \Phi^p = \int_{\Omega^p} \Sigma \delta\zeta d\Omega^p \tag{C.1}$$

where Ω^p is the plastic domain. The variation of the plastic energy density is:

$$\delta_\zeta \psi^p = \frac{\partial \psi^p}{\partial \zeta} \delta\zeta + \frac{\partial \psi^p}{\partial \nabla\zeta} : \delta\nabla\zeta \tag{C.2}$$

Therefore,

$$\delta\Phi^p = \delta \int_{\Omega^p} \psi^p d\Omega^p = \int_{\Omega^p} \frac{\partial \psi^p}{\partial \zeta} \delta\zeta d\Omega^p + \int_{\Omega^p} \frac{\partial \psi^p}{\partial \nabla\zeta} : \delta\nabla\zeta d\Omega^p \tag{C.3}$$

Integrating by parts and applying Green's theorem gives,

$$\int_{\Omega^p} \frac{\partial \psi^p}{\partial \nabla\zeta} : \delta\nabla\zeta d\Omega = \int_{\partial\Omega^p} \left(\frac{\partial \psi^p}{\partial \nabla\zeta} \cdot \boldsymbol{n_p}\right)\delta\zeta dS - \int_{\Omega^p} \left(\nabla \cdot \frac{\partial \psi^p}{\partial \nabla\zeta}\right)\delta\zeta d\Omega \tag{C.4}$$

where $\boldsymbol{n_p}$ is the outward normal of the elastic–plastic boundary $\partial\Omega^p$. As a result,

$$\Sigma\left(\zeta, \nabla^2\zeta\right) = \delta_\zeta \Phi^p = \sigma_y^0 + H\zeta - \beta {l_p}^2 \nabla^2\zeta \tag{C.5}$$

Due to the randomness of $\delta\zeta$, an additional boundary condition of $\frac{\partial \psi^p}{\partial \nabla\zeta} \cdot \boldsymbol{n_p} = \boldsymbol{0}$ should be fulfilled on the entire boundary $\partial\Omega^p$. The classic yield condition is employed here,

$$f\left(\sigma, c, \zeta, \nabla^2\zeta\right) = \sqrt{\boldsymbol{s} : \boldsymbol{s}} - \sqrt{\frac{2}{3}}\Sigma = \|\boldsymbol{s}\| - \sqrt{\frac{2}{3}}\left(\sigma_y^0 + H\zeta - \beta {l_p}^2 \nabla^2\zeta\right) \tag{C.6}$$

where $\boldsymbol{s} = \boldsymbol{\sigma} - \sigma_h \boldsymbol{1}$ is the deviatoric part of the stress tensor $\boldsymbol{\sigma}$. The plastic strain rate tensor is provided by a standard flow rule:

$$\dot{\boldsymbol{\varepsilon}}^p = \dot{\gamma}\frac{\partial g}{\partial \boldsymbol{\sigma}} \tag{C.7}$$

where g is the plastic flow potential, and $\dot{\gamma}$ is the rate of the plastic multiplier. Since plastic deformation is an irreversible process, the multiplier must be non-negative. For the associative flow rule $g = f$ and $\frac{\partial g}{\partial \boldsymbol{\sigma}} = f_{\boldsymbol{\sigma}} = \frac{\partial f}{\partial \boldsymbol{\sigma}} = \frac{\boldsymbol{s}}{\|\boldsymbol{s}\|} = \boldsymbol{n}$. The Kuhn–Tucker condition must be satisfied:

$$\dot{f} \le 0, \dot{\gamma} \ge 0, \dot{\gamma}\dot{f} = 0 \tag{C.8}$$

When plasticity takes place, $\dot{f} = 0$, hence

$$\dot{f} = \frac{\partial f}{\partial \boldsymbol{\sigma}} : \dot{\boldsymbol{\sigma}} + \frac{\partial f}{\partial \zeta}\dot{\zeta} + \frac{\partial f}{\partial \nabla^2\zeta}\nabla^2\dot{\zeta} + \frac{\partial f}{\partial c^*}\dot{c}^* = 0 \tag{C.9}$$

The last term accounts for chemical hardening/softening effects induced by changes in the chemical composition. For the time being, the chemical effect is neglected, i.e., $\frac{\partial f}{\partial c^*} = 0$. The effective plastic strain rate can be expressed by:

$$\dot{\zeta} = \sqrt{\frac{2}{3}\dot{\boldsymbol{\varepsilon}}^p : \dot{\boldsymbol{\varepsilon}}^p} = \sqrt{\frac{2}{3}}\dot{\gamma} \tag{C.10}$$

As a result,

$$\boldsymbol{n} : \mathbb{C}^e : (\dot{\boldsymbol{\varepsilon}} - \dot{\gamma}\boldsymbol{n}) - \frac{2}{3}H\dot{\gamma} + \frac{2}{3}\beta {l_p}^2 \nabla^2\dot{\gamma} = 0 \tag{C.11}$$

The weak form of the above can be written as:

$$\int_{\Omega^p} \boldsymbol{n} : \mathbb{C}^e : (\dot{\boldsymbol{\varepsilon}} - \dot{\boldsymbol{n}})\delta\dot{\gamma} dV - \int_{\Omega^p} \frac{2}{3}H\dot{\gamma}\delta\dot{\gamma} dV + \int_{\Omega^p} \frac{2}{3}\beta {l_p}^2 \nabla^2\dot{\gamma}\delta\dot{\gamma} dV = 0 \tag{C.12}$$

By applying Green's theorem,

$$\int_{\Omega^p} \frac{2}{3}\beta {l_p}^2 \nabla^2\dot{\gamma}\delta\dot{\gamma} dV = -\int_{\Omega^p} \frac{2}{3}\beta {l_p}^2 \nabla\dot{\gamma} \cdot (\nabla\delta\dot{\gamma}) dV + \int_{\partial\Omega^p} \frac{2}{3}\beta {l_p}^2 \left(\nabla\dot{\gamma} \cdot \boldsymbol{n}_\gamma\right)\delta\dot{\gamma} dS \tag{C.13}$$

where $\boldsymbol{n}_\gamma$ is the outward unit normal to the elastic–plastic boundary $\partial\Omega^p$. The following boundary conditions should be satisfied:

$$\delta\dot{\gamma} = 0 \text{ on } \Gamma_D^P \tag{C.14}$$

$$\nabla\dot{\gamma} \cdot \boldsymbol{n}_\gamma = 0 \text{ on } \Gamma_N^P \tag{C.15}$$

The Dirichlet elastic–plastic boundary Γ_D^P and Neumann elastic–plastic boundary Γ_N^P should satisfy: $\Gamma_D^P \cup \Gamma_N^P = \partial\Omega^p$, $\Gamma_D^P \cap \Gamma_N^P = \emptyset$. Typically, $\dot{\gamma} = 0$ is enforced on Γ_D^P. The final weak form can be given by:

$$\int_{\Omega^p} \boldsymbol{n} : \mathbb{C}^e : \dot{\boldsymbol{\varepsilon}}\delta\dot{\gamma} dV - \int_{\Omega^p} \left(2\Lambda + \frac{2}{3}H\right)\dot{\gamma}\delta\dot{\gamma} dV - \int_{\Omega^p} \frac{2}{3}\beta {l_p}^2 \nabla\dot{\gamma} \cdot (\nabla\delta\dot{\gamma}) dV = 0 \tag{C.16}$$

Appendix D. Numerical implementation of the model for elasto-plastic materials

The problem becomes to seek solutions of ${c_{n+1}}^*$, μ_{n+1}, u_{n+1}, and γ_{n+1} at the time step t_{n+1} given that ${c_n}^*$, μ_n, u_n, and γ_n at the time step t_n are known. Since the diffusion equation is the same as in the elastic case, ${c_{n+1}}^*$ and μ_{n+1} can be solved by the same approach. In order to solve for the increment of the consistency parameter, Eq. (44) can be discretized as:

$$\boldsymbol{n} : \mathbb{C}^e : \Delta\boldsymbol{\varepsilon}_n = \frac{4\Lambda}{\sqrt{6}}\left(\frac{\partial \Delta u_n}{\partial r} - \frac{\Delta u_n}{r}\right)\text{sign}\left({\left(\sigma_r\right)_n}'\right) \tag{D.1}$$

As a result, Eq. (C.16) can be rewritten as:

$$\int_0^1 \frac{4\Lambda}{\sqrt{6}}\left(\frac{\partial \Delta u_n}{\partial r} - \frac{\Delta u_n}{r}\right)\text{sign}\left({\left(\sigma_r\right)_n}'\right)\delta\gamma dr - \int_0^1 \left(2\Lambda + \frac{2}{3}H\right)\Delta\gamma_n\delta\gamma dV - \int_0^1 \frac{2}{3}\beta {l_p}^2 \nabla\frac{d\left(\Delta\gamma_n\right)}{dr} \cdot \frac{d\left(\delta\gamma\right)}{dr} dr = 0 \tag{D.2}$$

where

$$\Delta u_n = u_{n+1} - u_n,$$
$$\left(\sigma_r\right)_n' = \frac{2}{3}\left[\left(\sigma_r\right)_n - \left(\sigma_\theta\right)_n\right],\ \left(\sigma_\theta\right)_n' = -\frac{1}{3}\left[\left(\sigma_r\right)_n - \left(\sigma_\theta\right)_n\right],$$
$$\left(\sigma_e\right)_n = \left|\left(\sigma_r\right)_n - \left(\sigma_\theta\right)_n\right|,$$
$$\bar{\sigma}_n = \sigma_y^0 + H\left(\bar{\varepsilon}_p\right)_n,$$
$$\left(\bar{\varepsilon}_p\right)_n = \sqrt{\frac{2}{3}\left(\boldsymbol{\varepsilon}^p\right)_n : \left(\boldsymbol{\varepsilon}^p\right)_n},$$
$$\|\boldsymbol{s}\|_n = \sqrt{\frac{2}{3}}\left(\sigma_e\right)_n,\ \left(\Delta{\varepsilon_r}^p\right)_n = \Delta\gamma_n\frac{\left(\sigma_r\right)_n'}{\|\boldsymbol{s}\|_n},\ \left(\Delta{\varepsilon_\theta}^p\right)_n = \Delta\gamma_n\frac{\left(\sigma_\theta\right)_n'}{\|\boldsymbol{s}\|_n}.$$

As a result,

$$\gamma_{n+1} = \Delta\gamma_n + \gamma_n,$$
$$\left({\varepsilon_r}^p\right)_{n+1} = \left(\Delta{\varepsilon_r}^p\right)_n + \left({\varepsilon_r}^p\right)_n,$$
$$\left({\varepsilon_\theta}^p\right)_{n+1} = \left(\Delta{\varepsilon_\theta}^p\right)_n + \left({\varepsilon_\theta}^p\right)_n,$$

and the other quantities at time step t_{n+1} can also be computed. The mechanical equilibrium equation is essentially the same as for the elastic case, and the same solver is used. Once the internal iterations for solving the weak form of the mechanical equilibrium equation (Eq. (A.10)) converge, one increment of the mechanical field can be obtained by the forward Euler integration method. Thus, the mechanical equilibrium equation can be solved, and the stress field can be obtained incrementally.

Appendix E. Supplementary data

Supplementary material related to this article can be found online at https://doi.org/10.1016/j.ijmecsci.2021.106917.

References

[1] Choi D, Kumta PN. Surfactant based sol–gel approach to nanostructured LiFePO4 for high rate Li-ion batteries. J Power Sources 2007;163(2):1064–9.

[2] Li H, Huang X, Chen L, Wu Z, Liang Y. A high capacity nano Si composite anode material for lithium rechargeable batteries. Electrochem Solid-State Lett 1999;2(11):547–9.

[3] Liu XH, Zhong L, Huang S, Mao SX, Zhu T, Huang JY. Size-dependent fracture of silicon nanoparticles during lithiation. ACS Nano 2012;6(2):1522–31.

[4] Chew HB, Hou B, Wang X, Xia S. Cracking mechanisms in lithiated silicon thin film electrodes. Int J Solids Struct 2014;51(23–24):4176–87.

[5] Ryu I, Choi JW, Cui Y, Nix WD. Size-dependent fracture of si nanowire battery anodes. J Mech Phys Solids 2011;59(9):1717–30.

[6] Aifantis KE, Huang T, Hackney SA, Sarakonsri T, Yu A. Capacity fade in Sn–C nanopowder anodes due to fracture. J Power Sources 2012;197:246–52.

[7] Ma H, Cheng F, Chen J-Y, Zhao J-Z, Li C-S, Tao Z-L, et al. Nest-like silicon nanospheres for high-capacity lithium storage. Adv Mater 2007;19(22):4067–70.

[8] Choi HS, Lee JG, Lee HY, Kim SW, Park CR. Effects of surrounding confinements of Si nanoparticles on Si-based anode performance for lithium ion batteries. Electrochim Acta 2010;56(2):790–6.
[9] Yao Y, McDowell MT, Ryu I, Wu H, Liu N, Hu L, et al. Interconnected silicon hollow nanospheres for lithium-ion battery anodes with long cycle life. Nano Lett 2011;11(7):2949–54.
[10] McDowell MT, Ryu I, Lee SW, Wang C, Nix WD, Cui Y. Studying the kinetics of crystalline silicon nanoparticle lithiation with in situ transmission electron microscopy. Adv Mater 2012;24(45):6034–41.
[11] Wang JW, He Y, Fan F, Liu XH, Xia S, Liu Y, et al. Two-phase electrochemical lithiation in amorphous silicon. Nano Lett 2013;13(2):709–15.
[12] Ahuja U, Wang B, Hu P, Réthoré J, Aifantis KE. Polydopamine coated si nanoparticles allow for improved mechanical and electrochemical stability. Electrochim. Acta 2021;392:138993.
[13] Chan CK, Peng H, Liu G, McIlwrath K, Zhang XF, Huggins RA, et al. High-performance lithium battery anodes using silicon nanowires. Nature Nanotechnol 2008;3(1):31.
[14] Lee SW, McDowell MT, Choi JW, Cui Y. Anomalous shape changes of silicon nanopillars by electrochemical lithiation. Nano Lett 2011;11(7):3034–9.
[15] Liu N, Hu L, McDowell MT, Jackson A, Cui Y. Prelithiated silicon nanowires as an anode for lithium ion batteries. ACS Nano 2011;5(8):6487–93.
[16] Liu XH, Huang S, Picraux ST, Li J, Zhu T, Huang JY. Reversible nanopore formation in ge nanowires during lithiation–delithiation cycling: An in situ transmission electron microscopy study. Nano Lett 2011;11(9):3991–7.
[17] Park M-H, Kim MG, Joo J, Kim K, Kim J, Ahn S, et al. Silicon nanotube battery anodes. Nano Lett 2009;9(11):3844–7.
[18] Song T, Xia J, Lee J-H, Lee DH, Kwon M-S, Choi J-M, et al. Arrays of sealed silicon nanotubes as anodes for lithium ion batteries. Nano Lett 2010;10(5):1710–6.
[19] Liu Y, Zheng H, Liu XH, Huang S, Zhu T, Wang J, et al. Lithiation-induced embrittlement of multiwalled carbon nanotubes. ACS Nano 2011;5(9):7245–53.
[20] Mills E, Cannarella J, Zhang Q, Bhadra S, Arnold CB, Chou SY. Silicon nanopillar anodes for lithium-ion batteries using nanoimprint lithography with flexible molds. J Vac Sci Technol B 2014;32(6):06FG10.
[21] Kim G, Jeong S, Shin J-H, Cho J, Lee H. 3D Amorphous silicon on nanopillar copper electrodes as anodes for high-rate lithium-ion batteries. Acs Nano 2014;8(2):1907–12.
[22] Lee SW, McDowell MT, Berla LA, Nix WD, Cui Y. Fracture of crystalline silicon nanopillars during electrochemical lithium insertion. Proc Natl Acad Sci 2012;109(11):4080–5.
[23] Maranchi J, Hepp A, Kumta P. High capacity, reversible silicon thin-film anodes for lithium-ion batteries. Electrochem Solid-State Lett 2003;6(9):A198–201.
[24] Nadimpalli SP, Sethuraman VA, Bucci G, Srinivasan V, Bower AF, Guduru PR. On plastic deformation and fracture in si films during electrochemical lithiation/delithiation cycling. J Electrochem Soc 2013;160(10):A1885–93.
[25] Aifantis K, Hackney S. An ideal elasticity problem for Li-batteries. J Mech Behav Mater 2003;14(6):413–27.
[26] Aifantis KE, Dempsey J. Stable crack growth in nanostructured Li-batteries. J Power Sources 2005;143(1–2):203–11.
[27] Aifantis KE, Dempsey J, Hackney S. Fracture of nanostructured lithium batteries. In: Fracture of nano and engineering materials and structures. Springer; 2006, p. 63–4.
[28] Aifantis KE, Hackney S, Dempsey J. Design criteria for nanostructured Li-ion batteries. J Power Sources 2007;165(2):874–9.
[29] Dingreville R, Qu J, Cherkaoui M. Surface free energy and its effect on the elastic behavior of nano-sized particles, wires and films. J Mech Phys Solids 2005;53(8):1827–54.
[30] Cheng Y-T, Verbrugge MW. The influence of surface mechanics on diffusion induced stresses within spherical nanoparticles. J Appl Phys 2008;104(8):083521.
[31] Deshpande R, Cheng Y-T, Verbrugge MW. Modeling diffusion-induced stress in nanowire electrode structures. J Power Sources 2010;195(15):5081–8.
[32] Wang C, Ma Z, Wang Y, Lu C. Failure prediction of high-capacity electrode materials in lithium-ion batteries. J Electrochem Soc 2016;163(7):A1157–63.
[33] Kizuka T, Takatani Y, Asaka K, Yoshizaki R. Measurements of the atomistic mechanics of single crystalline silicon wires of nanometer width. Phys Rev B 2005;72(3):035333.
[34] Uchic MD, Dimiduk DM, Florando JN, Nix WD. Sample dimensions influence strength and crystal plasticity. Science 2004;305(5686):986–9.
[35] Michler J, Wasmer K, Meier S, Östlund F, Leifer K. Plastic deformation of gallium arsenide micropillars under uniaxial compression at room temperature. Appl Phys Lett 2007;90(4):043123.
[36] Gerberich WW, Michler J, Mook W, Ghisleni R, Östlund F, Stauffer D, et al. Scale effects for strength, ductility, and toughness in "brittle" materials. J Mater Res 2009;24(3):898–906.
[37] Hao F, Fang D. Diffusion-induced stresses of spherical core-shell electrodes in lithium-ion batteries: the effects of the shell and surface/interface stress. J Electrochem Soc 2013;160(4):A595–600.
[38] Christensen J, Newman J. Stress generation and fracture in lithium insertion materials. J Solid State Electrochem 2006;10(5):293–319.
[39] Verbrugge MW, Cheng Y-T. Stress and strain-energy distributions within diffusion-controlled insertion-electrode particles subjected to periodic potential excitations. J Electrochem Soc 2009;156(11):A927–37.
[40] Deshpande R, Qi Y, Cheng Y-T. Effects of concentration-dependent elastic modulus on diffusion-induced stresses for battery applications. J Electrochem Soc 2010;157(8):A967–71.
[41] Cheng Y-T, Verbrugge MW. Diffusion-induced stress, interfacial charge transfer, and criteria for avoiding crack initiation of electrode particles. J Electrochem Soc 2010;157(4):A508–16.
[42] Song Y, Lu B, Ji X, Zhang J. Diffusion induced stresses in cylindrical lithium-ion batteries: analytical solutions and design insights. J Electrochem Soc 2012;159(12):A2060–8.
[43] Zhang J, Lu B, Song Y, Ji X. Diffusion induced stress in layered Li-ion battery electrode plates. J Power Sources 2012;209:220–7.
[44] Bhandakkar TK, Johnson HT. Diffusion induced stresses in buckling battery electrodes. J Mech Phys Solids 2012;60(6):1103–21.
[45] Li J, Fang Q, Liu F, Liu Y. Analytical modeling of dislocation effect on diffusion induced stress in a cylindrical lithium ion battery electrode. J Power Sources 2014;272:121–7.
[46] Cheng Y-T, Verbrugge MW. Evolution of stress within a spherical insertion electrode particle under potentiostatic and galvanostatic operation. J Power Sources 2009;190(2):453–60.
[47] Prussin S. Generation and distribution of dislocations by solute diffusion. J Appl Phys 1961;32(10):1876–81.
[48] Deshpande R, Cheng Y-T, Verbrugge MW, Timmons A. Diffusion induced stresses and strain energy in a phase-transforming spherical electrode particle. J Electrochem Soc 2011;158(6):A718–24.
[49] Haftbaradaran H, Maddahian A, Mossaiby F. A fracture mechanics study of the phase separating planar electrodes: Phase field modeling and analytical results. J Power Sources 2017;350:127–39.
[50] Walk A-C, Huttin M, Kamlah M. Comparison of a phase-field model for intercalation induced stresses in electrode particles of lithium ion batteries for small and finite deformation theory. Eur J Mech A Solids 2014;48:74–82.
[51] Huang S, Fan F, Li J, Zhang S, Zhu T. Stress generation during lithiation of high-capacity electrode particles in lithium ion batteries. Acta Mater 2013;61(12):4354–64.
[52] Chen L, Fan F, Hong L, Chen J, Ji Y, Zhang S, et al. A phase-field model coupled with large elasto-plastic deformation: application to lithiated silicon electrodes. J Electrochem Soc 2014;161(11):F3164–72.
[53] Chang L, Lu Y, He L, Ni Y. Phase field model for two-phase lithiation in an arbitrarily shaped elastoplastic electrode particle under galvanostatic and potentiostatic operations. Int J Solids Struct 2018;143:73–83.
[54] Sethuraman VA, Chon MJ, Shimshak M, Van Winkle N, Guduru PR. In situ measurement of biaxial modulus of Si anode for Li-ion batteries. Electrochem Commun 2010;12(11):1614–7.
[55] Shuang F, Aifantis KE. A first molecular dynamics study for modeling the microstructure and mechanical behavior of Si nanopillars during lithiation. ACS Appl Mater Interfaces 2021. In print.
[56] Liu Y, Lv P, Ma J, Bai R, Duan HL. Stress fields in hollow core–shell spherical electrodes of lithium ion batteries. Proc R Soc A 2014;470(2172):20140299.
[57] Lu Y, Soh AK, Ni Y, He L. Understanding size-dependent migration of a two-phase lithiation front coupled to stress. Acta Mech 2019;230(1):303–17.
[58] Aifantis EC. On the role of gradients in the localization of deformation and fracture. Internat J Engrg Sci 1992;30(10):1279–99.
[59] Aifantis EC. Update on a class of gradient theories. Mech Mater 2003;35(3–6):259–80.
[60] Aifantis EC. A concise review of gradient models in mechanics and physics. Front Phys 2020;7:239.
[61] Aifantis EC. On the microstructural origin of certain inelastic models. 1984.
[62] Aifantis EC. Internal length gradient (ILG) material mechanics across scales and disciplines. Adv Appl Mech 2016;49:1–110.
[63] Fleck N, Hutchinson J. A phenomenological theory for strain gradient effects in plasticity. J Mech Phys Solids 1993;41(12):1825–57.
[64] Fleck N, Muller G, Ashby MF, Hutchinson JW. Strain gradient plasticity: theory and experiment. Acta Metall Mater 1994;42(2):475–87.
[65] Aifantis K, Soer W, De Hosson JTM, Willis J. Interfaces within strain gradient plasticity: theory and experiments. Acta Mater 2006;54(19):5077–85.
[66] Tsagrakis I, Aifantis EC. Gradient elasticity effects on the two-phase lithiation of LIB anodes. In: Generalized models and non-classical approaches in complex materials 2. Springer; 2018, p. 221–35.
[67] Tsagrakis I, Konstantopoulos I, Sidiropoulos A, Aifantis EC. On certain applications of gradient nanochemomechanics: deformation and fracture of LIB and SGS. J Mech Behav Mater 2019;28(1):74–80.
[68] Natarajan S, Aifantis K. Size effects in nanostructured Li-ion battery cathode particles. J Mech Behav Mater 2020;29(1):36–43.
[69] Dimitrijevic B, Aifantis KE, Hackl K. The influence of particle size and spacing on the fragmentation of nanocomposite anodes for Li batteries. J Power Sources 2012;206:343–8.
[70] Yamada A, Koizumi H, Sonoyama N, Kanno R. Phase change in Li x FePO4. Electrochem Solid-State Lett 2005;8(8):A409–13.

[71] Wang D, Wu X, Wang Z, Chen L. Cracking causing cyclic instability of LiFePO4 cathode material. J Power Sources 2005;140(1):125–8.
[72] Belytschko T, Bažant ZP, Yul-Woong H, Ta-Peng C. Strain-softening materials and finite-element solutions. Comput Struct 1986;23(2):163–80.
[73] Jirásek M. Objective modeling of strain localization. Rev Fr Génie Civ 2002;6(6):1119–32.
[74] Bazant ZP, Planas J. Fracture and size effect in concrete and other quasibrittle materials, Vol. 16. CRC Press; 1997.
[75] Rogers SO, Bendich AJ. Extraction of DNA from plant tissues. In: Plant molecular biology manual. Springer; 1989, p. 73–83.
[76] Jirasek M. Nonlocal models for damage and fracture: comparison of approaches. Int J Solids Struct 1998;35(31–32):4133–45.
[77] Planas J, Elices M, Guinea G. Cohesive cracks versus nonlocal models: Closing the gap. Int J Fract 1993;63(2):173–87.
[78] Aifantis EC. The physics of plastic deformation. Int J Plast 1987;3(3):211–47.
[79] Gurtin ME, Murdoch AI. A continuum theory of elastic material surfaces. Arch Ration Mech Anal 1975;57(4):291–323.
[80] Gurtin ME, Me G, Ai M. Surface stress in solids.. 1978.
[81] Zhao X, Bordas SP, Qu J. Equilibrium morphology of misfit particles in elastically stressed solids under chemo-mechanical equilibrium conditions. J Mech Phys Solids 2015;81:1–21.
[82] Shen S, Hu S. A theory of flexoelectricity with surface effect for elastic dielectrics. J Mech Phys Solids 2010;58(5):665–77.
[83] Miehe C, Hildebrand F, Böger L. Mixed variational potentials and inherent symmetries of the Cahn–Hilliard theory of diffusive phase separation. Proc R Soc A 2014;470(2164):20130641.
[84] Martínez-Pañeda E, Golahmar A, Niordson CF. A phase field formulation for hydrogen assisted cracking. Comput Methods Appl Mech Engrg 2018;342:742–61.
[85] Lou Y, Bassani JL. Guided assembly of nanostructures via elastic interactions. J Mech Phys Solids 2008;56(12):3507–26.
[86] Tonks MR, Gaston D, Millett PC, Andrs D, Talbot P. An object-oriented finite element framework for multiphysics phase field simulations. Comput Mater Sci 2012;51(1):20–9.
[87] Wodo O, Ganapathysubramanian B. Computationally efficient solution to the Cahn–Hilliard equation: Adaptive implicit time schemes, mesh sensitivity analysis and the 3D isoperimetric problem. J Comput Phys 2011;230(15):6037–60.
[88] Zaeem MA, Mesarovic SD. Finite element method for conserved phase fields: Stress-mediated diffusional phase transformation. J Comput Phys 2010;229(24):9135–49.
[89] Hofmann T, Westhoff D, Feinauer J, Andrä H, Zausch J, Schmidt V, et al. Electro-chemo-mechanical simulation for lithium ion batteries across the scales. Int J Solids Struct 2020;184:24–39.
[90] Chen Q, Pugno N, Li Z. Influence of surface stress on elastic constants of nanohoneycombs. Physica E 2013;53:217–22.
[91] Miller RE, Shenoy VB. Size-dependent elastic properties of nanosized structural elements. Nanotechnology 2000;11(3):139.
[92] Gurtin ME, Weissmüller J, Larche F. A general theory of curved deformable interfaces in solids at equilibrium. Phil Mag A 1998;78(5):1093–109.
[93] Bai P, Cogswell DA, Bazant MZ. Suppression of phase separation in LiFePO4 nanoparticles during battery discharge. Nano Lett 2011;11(11):4890–6.
[94] Wang B, Réthoré J, Aifantis KE. Capturing the stress evolution in electrode materials that undergo phase transformations during electrochemical cycling. Int J Solids Struct 2021;224:111032.
[95] Altan S, Aifantis E. On the structure of the mode III crack-tip in gradient elasticity. Scr Metall Mater 1992;26(2):319–24.
[96] Vardoulakis I, Georgiadis H. SH surface waves in a homogeneous gradient-elastic half-space with surface energy. J Elasticity 1997;47(2):147–65.
[97] Liu XH, Fan F, Yang H, Zhang S, Huang JY, Zhu T. Self-limiting lithiation in silicon nanowires. Acs Nano 2013;7(2):1495–503.
[98] Liu XH, Wang JW, Huang S, Fan F, Huang X, Liu Y, et al. In situ atomic-scale imaging of electrochemical lithiation in silicon. Nature Nanotechnol 2012;7(11):749–56.
[99] Cui L-F, Ruffo R, Chan CK, Peng H, Cui Y. Crystalline-amorphous core- shell silicon nanowires for high capacity and high current battery electrodes. Nano Lett 2009;9(1):491–5.
[100] Chon MJ, Sethuraman VA, McCormick A, Srinivasan V, Guduru PR. Real-time measurement of stress and damage evolution during initial lithiation of crystalline silicon. Phys Rev Lett 2011;107(4):045503.
[101] Deng H, Chu G, Luo F, Li H, Chen L, Aifantis KE. Si micropyramid patterned anodes that can suppress fracture and solid electrolyte interface formation during electrochemical cycling. J Power Sources 2016;329:372–8.
[102] Pennelli G, Totaro M, Nannini A. Correlation between surface stress and apparent Young's modulus of top-down silicon nanowires. ACS Nano 2012;6(12):10727–34.
[103] Kristensen PK, Niordson CF, Martínez-Pañeda E. A phase field model for elastic-gradient-plastic solids undergoing hydrogen embrittlement. J Mech Phys Solids 2020;143:104093.
[104] https://fenics-dolfin.readthedocs.io/en/2017.2.0/apis/api_nls.html.